For submission to Chemical Geology

The effect of fO_2 on the diffusion of redox-sensitive elements in haplobasaltic melt at 1 GPa and 1300 °C

Ian Szumila[a,b] Dustin Trail[a,c], Lisa Danielson[b]*

[a]Department of Earth & Environmental Sciences
University of Rochester, Rochester, NY 14627

[b]Jacobs - JETS, JSC, 2224 Bay Area Blvd, Houston, TX, 77058

[c]Department of Earth, Planetary and Space Sciences,
University of California, Los Angeles, CA, 90095, USA

iszumila@ur.rochester.edu ; ph 214 287 8227

Keywords: diffusion, redox, oxygen fugacity, basalt, planetary, Europium

ABSTRACT

Diffusivities for elements (P, Sc, V, Mn, Co, Zn, Cr, Nb, Mo, La, Ce, Pr, Sm, Eu, Gd, Ta, W) at 1300 °C and 1 GPa in basaltic melts were characterized across a range of oxygen fugacity (fO_2) conditions. Experiments were carried out using either a reducing (FMQ-3.1), intermediate (~FMQ-1.2) or oxidizing (FMQ+6) fO_2. For each fO_2, three experiments were conducted for durations of 20, 40, and 80 minutes. For a given time series, changes in diffusivity are typically within 3 standard error at a single fO_2. The magnitudes of the elemental diffusivities can be grouped into those of the High-field Strength Elements (HFSE), the Rare Earth Elements (REE), the transition elements, and P. Vanadium and Sc have diffusivities more similar to the REEs and HFSEs respectively, than the other transition elements. The best fits of diffusivities for P also suggest that the diffusivity of this element is more in line with the HFSE. At oxidizing conditions, a fractionation of Nb from Ta with greater magnitude than that at the other oxygen fugacities is seen. Across oxygen fugacities explored here, Eu exhibits unique changes in diffusion. At more reducing conditions, the diffusivity of Eu increases relative to the neighboring REE elements Sm and Gd, with this effect most pronounced at FMQ-3.1 and present in experiments conducted at intermediate fO_2 conditions. This demonstrates that an Eu anomaly can be generated by diffusion alone. In oxidizing conditions, because Eu likely is present as mostly Eu^{3+}, the signal vanishes as Eu diffusivity becomes similar to that of other trivalent REEs. There are small systematic changes in element diffusivities for both redox-sensitive and non-redox sensitive elements as fO_2 is varied. Averages of the 20, 40, and 80 minute diffusivities for all elements done in the intermediate fO_2 experiments have the slowest diffusivities of the three oxygen fugacities explored. On average, the diffusivities of the entire contingent of elements studied from the more reducing (FMQ-3.1) conditions are faster than those from the intermediate fO_2 by about a factor of 1.5. The elemental diffusivities recovered from the oxidizing experiments are, on average, about ~2 times as fast of those recovered from the intermediate experiments. For elements fit in these experiments, an order of magnitude change in element diffusivities, even for redox-sensitive elements, is never seen over the range of oxygen fugacities explored at 1300 °C. These experiments demonstrate that oxygen fugacity can have an important effect on the diffusivity of certain redox-sensitive elements (e.g. Eu) and that fO_2 may play a role in element transport generally.

1. Introduction

Oxygen fugacity (fO_2) is an important intensive magmatic variable that can influence mineral assemblages present (Carmichael and Ghiosro, 1990; Diener and Powell, 2010; Hensen, 1986) and the valence and partitioning of major and trace elements in minerals and co-existing melts (Burnham and Berry, 2012; Shearer et al, 2006; Trail et al., 2011; Wilke and Behrens, 1999). Diffusion may also play major roles in crystal growth or fractionation of elements. For a crystal growing in melt, element uptake at the boundary layer can be affected by diffusivities of different elements, and probably causes fractionations between elements based on ion size and charge. (Watson and Müller, 2009). Several useful geochemical tracers depend on element ratios which may depend on a redox-sensitive element (e.g. V/Sc in Mallmann and O'Neill. 2009, Zn/Fe_T in Lee et al. 2010, or Ce/Ce* in Trail et al. 2011) Because of this, fractionation by diffusion due to fO_2 may affect their use and ultimate meaning. Vanadium, for example, has several redox states, (e.g. V^{2+}, V^{3+}, V^{4+}, V^{5+}) which makes it useful for studying fO_2 across a broad range of solar system conditions (Mallmann and O'Neill, 2009; Shearer et al, 2006). In addition, V/Sc and V/Ga ratios have been used to investigate the differences in oxidation between arc basalts, ocean island basalt (OIB) and mid-ocean ridge basalt (MORB), and to suggest that the mantle sources have indistinguishable redox conditions for both arc basalts and MORB (Mallmann and O'Neill, 2009) although other work involving the olivine-spinel oxybarometry by Evans et al. (2012) argues for a subarc mantle that is more oxidized than either OIB or MORB source regions. Measurements of V/Sc indicate that fO_2 for MORB source is constrained to FMQ-0.3±0.5 (Li and Lee, 2004). The V/(Cr+Al) ratio has also been used to compare fO_2 of planetary materials via chromite grains (Papike et al, 2004). Most rare earth elements (REEs), have only trivalent valence states in natural settings. The two exceptions to this are Ce, which has 3+ and 4+ states

and Eu with 2+ and 3+ states. These properties have made the REEs useful in studying the oxidation state of minerals and magmas. For example, partitioning of the redox-sensitive elements Ce and Eu between melt and zircons can be used to study the oxidation state of magmas (Trail et al, 2012).

Table 1 show dominant redox states of different elements at the varying oxygen fugacity used in these experiments. Elements such as V have the dominant valence state varying nearly systematically over the three fO_2s used in these experiments. Iron is similar being present as Fe^{2+} in the two reducing conditions but oxidized to Fe^{3+} under the Ru-RuO_2 (RRO) buffer. The 4+ state of the Ce is known to only be present in vary small amounts in basaltic melts as it will complex with Fe^{2+} to form Fe^{3+}-O-Ce^{3+} (Schreiber et al, 1980). Niobium and Ta are most likely only pentavalent over the redox range used here. Tantalum speciation is not calibrated for RRO (Burnham et al, 2012), though 5+ is reasonable since a more oxidized valence for that element is not known. Phosphorus is only ever found in the redox states of P^{5+} and P^0 although Mallmann and O'Neill (2009) present some evidence for P^{3+} at reducing conditions. Molybdenum is present as Mo^{6+} when studied experimentally in basalts above iron-wüstite (IW-1; equivalent to FMQ-4.45 or MMO-1.4 at 1300 ℃) yet is often found in nature in the tetravalent state, as molybdenite (Farges et al., 2006). Papike et al (2004), places Eu^{3+} has the dominant redox state of Eu over the fO_2 conditions used in these experiments.. Although this does not preclude there being an increasing amount of Eu^{2+} as more reducing conditions are approached.

Terrestrial planetary bodies – including the Moon and some differentiated asteroids – produce basalts. Since these bodies have experienced the melting and differentiation processes over different fO_2s, understanding how diffusivities of elements change with varying fO_2 will enhance our understanding of material transport by diffusion. While typical MORBs analyzed by Cottrell et al. (2011) show a restricted range in fO_2 of FMQ+0.10 $\pm$0.18, surface material on Earth has experienced melting conditions that have resulted in a much wider range of fO_2s. Basalt erupted on Disko Island yielded an fO_2 of IW due to interaction with graphite during eruption (Bird and Weathers, 1977; Goodrich and Bird, 1985). The Earth can also produce highly oxidized material; arc basalts, for example, approach FMQ+4.0 (Gaillard et al, 2015). Martian Fe-Ti oxides in shergottites record oxygen fugacities between FMQ-1 and FMQ-3 (Herd et al., 2002). Sato et al. (1973) analyzed lunar samples including basalts (12009, 12022, 12053, 15058, 15595), a microbreccia, (14321) and a basaltic rock (14310) which has been identified (Duncan et al, 1975) as a surficial impact melt. They found the bulk rock fO_2 of the lunar basalts, the Apollo 12 and 15 samples, they studied to be $10^{-12.3}$ to $10^{-12.8}$ at 1200 ℃ or IW-0.36 to IW-0.86 respectively. The Howardite, Eucrite, and Diogenite (HED) meteorites, have spectral similarities to the asteroid Vesta 4 (McCord et al., 1970) and more recent mission work from the Dawn mission (Russell et al, 2012) continues to support this hypothesis by reporting on the mineralogy of the Vestan surface and a large basin that could have sourced the HEDs. Based on models of Si isotope work in HEDs (Pringle et al, 2013), Vesta 4 differentiated around IW-4.2$\pm$0.1, while other models which incorporate partitioning of siderophile elements and HED meteorite analyses (Steenstra et al., 2016), place the fO_2 at differentiation as IW-2.15$\pm$0.30.

In past studies, Nakamura and Kushiro (1998) characterized the diffusion of elements in jadeite and albite melt and discussed how a zoned magma chamber could lead to the formation of an Eu anomaly under reducing conditions, or depletions and enrichments of the Rare Earth Elements (REEs). Previous workers have characterized trace element diffusivities at a single fO_2 with varying T (e.g. Holycross and Watson, 2016), or examined how the properties of one or two select elements are affected by a change in redox and T (e.g. Sn in Linnen et al, 1995; P in Watson et al, 2015) Others have done interesting geochemical research on topics like partitioning (e.g. Nb and Ta in Cartier et al, 2014).Diffusivities of several trace elements from many different works are characterized for silicate melts in Zhang et al. (2010), but not all elements have been studied using a MORB-like composition. So to add to this body of knowledge, we conducted systematic study that characterizes diffusivities of redox sensitive elements vs. fO_2 in basalts. Here we report changes in element diffusivities as fO_2 is varied. We demonstrate that redox-sensitive elements may be fractionated by diffusion, and that the magnitude of this fractionation is fO_2 dependent. Moreover, significant changes in fO_2 leads to small but detectable changes in the diffusivity of non-redox sensitive elements, possibly due to fO_2 -induced changes in melt structure.

2. Materials and Methods

2.1 Rock Mixes

Our strategy for experiments was to set up diffusion couples in capsules inside the piston cylinder for each oxygen fugacity. This entailed the production of both low-trace element and a high-trace element basalts material for use in each side of the diffusion couple.

Thus, a major element base mix and a separate trace element mix were prepared using reagent grade materials. All Fe was added as FeO (99.5% pure), while Na, K, and Ca were added as Na_2CO_3, K_2CO_3 and $CaCO_3$ respectively. **Table 2** shows the major weight % composition targets and the compositions of actual experiments as analyzed by a JEOL 8350F electron microprobe with instrument conditions discussed in section 2.4. The trace mix was made with consideration of the chondritic abundance of each element (Anders and Grevasse, 1989; Barrat et al., 2012; Elardo et al., 2011; Pourmand et al., 2012; Ruzicka et al., 2000). This involved elements that were not enriched at all compared to chondritic abundances, such as P, Sc, V, Co, Mn, Ni, Cu, and Zn. Other Elements (i.e. Nb, La, Ce, Pr, Sm, Eu, Gd, Ta, W) whose low chondritic abundances would have made them difficult to analyze were enriched by a factor of 1000. The ratios of any two unenriched trace elements is broadly the same as chondrite while the same is also true of the ratio of any two enriched elements. Finally, because of the high abundance of Cr and tendency to form spinels, a ppm level of 100 was targeted rather than the original relative chondritic amount. The targeted wt% level of each component making up the trace is shown in **Table 3**. Elements that were enriched are marked with an asterisk in **Table 3**. In addition to material already present in the base mix, the trace mix contained additional K_2CO_3 and TiO_2.

The base and trace mixes were ground individually by hand in a mortar and pestle for 15 minutes. Three base mixtures of ~5 g were generated for each fO_2. The base mix for a given fO_2 was divided in two, and then mixed with 0.1 wt% and 0.5 wt% of the trace mix to create high-trace element and low-trace element basalt mixes. The six mixes were individually heated to 800 ℃ and left in a furnace for three hours for decarbonating.

2.2 One Atmosphere Glass Fusions

The rock mixes were then packed into a 30 ml Pt crucible, and fused in a DelTech 1 atmosphere CO-CO_2 gas mixing furnace at 1350 ℃ for 24 hours. Two fusions, with high and low trace element compositions, were conducted at each of the 3 fO_2s designed to match the final fO_2 of the diffusion experiments. This resulted in a total of six 1-bar fusion sessions. During the fusion, temperature was monitored with a Type B thermocouple. After 24 hours, the crucible was drop-quenched into DI water, or if drop-quenching mechanism failed to engage then by removing and immediately dunking the crucible into a bucket of DI water. The glass was broken out of the Pt crucible, and then ground back into a powder by using an automatic mortar grinder for 25 minutes with the glass under an acetone slurry. For material to be used with MMO, or 1 GPa graphite capsule experiments, the fO_2 conditions of certain nearby buffers (i.e. IW and FMQ) were targeted directly by the CO-CO_2 gas mixture. For RRO, the fO_2 was too oxidizing for a CO-CO_2 atmosphere to reach, so instead a full CO_2 atmosphere (~FMQ+3.53 or ~RRO-2.25) was used to oxidize the starting material. The fO_2 inside the furnace was monitored by using an EMF sensor calibrated with a reference fO_2 cell.

During the 1 atmosphere synthesis step, it is expected that Fe and possibly Zn were lost to the Pt crucible when conditions near IW were imposed. The effects of this on the final composition can be viewed in **Table 2** and are explored further in the discussion section 4.5.

2.3 Piston Cylinder Diffusion Experiments and Buffers

After fusion, material was loaded into capsules for use in diffusion experiments. Capsules were made of either Mo, graphite, or 95%Pt-5%Ru. Molybdenum and graphite capsules serve the dual purpose

of constraining the fO_2. Mo metal, when present with MoO_2, buffers a sample close to IW (specifically IW+0.39) at 1300 °C. (ONeill, 1986; O'Neill and Pownceby, 1993) The Mo experiments were checked afterward for the presence of an oxidized Mo (i.e. MoO_2) phase in contact with the glass. At 1 GPa and 1300 °C, graphite, is expected to buffer a sample close to FMQ-1.2. This was calculated from a calibration done by Ulmer and Luth, (1991) who studied graphite in contact with a C-O-H fluid over fO_2 while keeping fH_2 fixed using the double capsule technique. The interior wells of all graphite and Mo capsules used were end-milled flat to limit the contributions of capsule geometry to diffusion. For the Mo and graphite capsules, the high trace elements material was always packed onto the bottom of the capsule, with a drill blank, then the low trace elements material was packed on top. This material on top was then also pushed down flat using the same drill blank. The packing was done this way based on the assumption that the higher trace element material was denser and that this method of packing might serve to minimize gravitational settling.

The Pt-Ru capsules are used when an oxidizing fO_2 is desired. The Pt-Ru capsules were made by sectioning a Pt-Ru tube to a length of 10 mm. Then one end of this tube was crimped shut and welded with an arc welder. A Ru-RuO_2 fO_2 buffer mixture, consisting of 1:20 (by weight), was then packed into the bottom of the capsule. This mix is heavily biased towards oxidizing material (Trail et al., 2012) since we expect piston cylinders to impose an intrinsic fO_2 closer to FMQ. The Ru-RuO_2 and the HM buffers are very similar at 1300 °C, with RRO being ~0.4 log units more oxidizing than HM. (Myers and Eugster, 1983; O'Neill and Nell, 1997) After loading this buffer material, the high-trace element basalt mix is loaded followed by the low-trace element basalt mix. Finally more buffer material is added to the top. The capsule was then crimped on the top and welded with an arc welder to fully seal the capsule. Ru and RuO_2 have low solubilities in basaltic melts (Bockrath et al., 2004; O'Neill and Nell, 1997) so although they are in direct contact with the melt, their expected effect on the experiment besides buffering fO_2 is minimal.

End-loaded piston cylinders at the University of Rochester were used for most experiments. One experiment was conducted with a Quik-press piston cylinder model used at NASA Johnson Space Center. Cross sections of a loaded Mo capsule, a loaded graphite capsule and a loaded Pt-Ru capsule used for experiments are shown in **Figure 1.** Filler pieces consisted of crushable MgO machined to the proper dimensions and loaded into a graphite furnace. Sleeves of MgO were used to surround the Mo and graphite capsules. For RRO-buffered experiments, the Pt-Ru capsule is placed in an MgO sleeve which is then subsequently filled with powdered MgO to fully surround the capsule. After placing the graphite furnace into pyrex glass and salt cells, the full assembly was pressurized in a piston cylinder to 1 GPa. All experiments were maintained at pressure for at least one hour before heating.

Samples were heated to 1300 °C with a ramp-time of seven minutes to the target temperature, correlating to a ramp rate of ~185 °C/minute. Both the end-loaded and Quik-press designs used a Type C, 25%WRe-3%WRe thermocouple to monitor the temperature. In the end-loaded design, the thermocouple wire is threaded through thermocouple insulator directly above the sample. For the Quik-press design, the wire is still threaded through thermocouple insulator but instead inserted directly below the sample. Experiments for each fO_2 condition explored were conducted as a time series, with dwell times at the target temperature of 20, 40 and 80 minutes. This helps to confirm that diffusion is the primary process responsible for mass transfer. Moreover, elements that diffused too quickly such that diffusivities are not recoverable for 80 minute experiments can still be fit for the shorter durations. In addition, 2 experiments (RRO and MMO) with dwell times of 90 seconds at ~1300 °C were conducted to understand how quickly buffering phases form or are consumed. After this dwell period ended, they were immediately quenched.

All experiments were retrieved by cutting the power to the piston cylinder, and quenching isobarically by using the pump to stave off pressure losses. All experiments cool to less than 100 °C in less than 40 seconds. After quenching, pressure on the sample was bled slowly back to atmosphere over 5 minutes. All experiments were then mounted in 1-inch epoxy rounds. For experiments prone to decompression cracking, particularly those done in graphite capsules, they were sanded with 400 grit sandpaper until the experimental glass became visible, and then vacuum impregnated with epoxy. This helped to prevent loss of sample or formation of very large decompression cracks. Then experimental products were sectioned with a low-speed diamond saw. Sectioned experiments including the capsule material are typically about 0.25 cm^2. While steps were taken to avoid decompression cracking during the

quenching of experiments, decompression cracks were common in experiments done with Pt-Ru or graphite capsules while very rare in those done with Mo capsules. After sectioning experiments, they were re-mounted in 1-inch epoxy rounds to make a new flat epoxy round centered on the face of the sample. After the epoxy set, the charges were polished by hand with 240, 400 and 600 grit sandpaper, and finished with 1 μm alumina on an automatic polisher for 30 minutes.

2.4 Scanning Electron Microscope (SEM) and Electron Microprobe (EMPA)

The RRO- and MMO-buffered samples were analyzed for the presence of buffering phases by the JEOL 7600F at NASA JSC SEM after carbon coating. An accelerating voltage of 15 kV to collect backscatter images and Energy-dispersive X-ray Spectroscopy (EDS) was used for quick investigations of various sample phases and to determine if a phase was oxidized.

Select MMO, RRO and graphite capsule experiments were also analyzed using the JEOL 8530F NASA JSC electron microprobe to quantify major element composition and compare to the target compositions of the base mix by Wave-length X-Ray Dispersive Spectroscopy (WDS). Analyses were conducted with an accelerating voltage was 15 kV, a beam current of 15 nA and a defocused beam diameter of 10 μm. The RRO experiment graphite capsule experiment were analyzed during the same session. For that session, Kα x-rays of Si, Al, Mg and Na were collected on TAP crystal while for Ti and K, a PETL crystal was used. X-rays from P and Ca were collected on a PET and the Mn on LIFH. Lα x-rays of Mo were collected on the same PETL crystal used for Ti and K. The MMO sample from Table 2 was analyzed during a later session which used a similar WDS crystal setup with the specific settings mentioned following for completeness. The Kα x-rays of Si, Al, Mg and Na were collected again with a TAP crystal while K was measured on a PET crystal. Titanium, and Mn, Fe, Ni were all measured using a LIFH crystal. The Lα x-rays of Mo were also analyzed via PET and the Lα of W collected on LIFL. Concentrations were calculated from natural and synthetic microprobe standards, including VG2 MORB from the Juan de Fuca ridge (Jarosewich et al., 1980), analyzed with the samples during the sessions. Corrections were done using the ZAF method.

2.5 Laser Ablation-Inductively Coupled Plasma- Mass Spectrometry (LA-ICP-MS)

Trace element diffusion profiles were measured with a Laser Ablation-Inductively Coupled Plasma-Mass Spectrometry (LA-ICP-MS) at the University of Rochester consisting of an Agilent 7900 quadrupole attached to a Photon Machines Analyte G2 ArF 193 nm laser. Repetition rate was set to 10 Hz. Fluence used for all analyses was 7.81 J/cm^2 with a spot size of 35 μm. The laser used a two volume HelEx sample cell with He gas flows kept at 0.6 L/min (MFC1) and 0.2 L/min (MFC2) during analysis Laser ablation spots were laid down with consistent spacing via the Chromium 2.0 software meaning that some spots occasionally ended up either entirely or partially on a decompression crack, which is dealt with during data reduction. Uncorrected distance between spots was 65-125 μm depending on analysis. Only one profile down the center of each sample from an analytical session was fitted to generate the diffusion profiles. Some experiments were analyzed again specifically for difficult to measure elements including P, Cr, Mn, Co, Zn, and Ni. Diffusivities presented are always from one of these analysis sessions.

Isotopes that were analyzed are ^{31}P, ^{45}Sc, ^{55}Mn, ^{59}Co, ^{66}Zn, ^{93}Nb, ^{95}Mo, ^{139}La, ^{140}Ce, ^{141}Pr, ^{147}Sm, ^{153}Eu, ^{157}Gd, ^{181}Ta, ^{182}W. Chromium was sometimes analyzed a ^{52}Cr isotope and sometimes as ^{53}Cr. For most analyses, ^{60}Ni or ^{63}Cu were included as well, ^{60}Ni was analyzed for everything except the 20 minute graphite capsule experiment and ^{63}Cu was analyzed for everything except the 20 minute RRO experiment. The isotope ^{29}Si was monitored for use as an internal standard.

2.6 Data Reduction and Calculation of Diffusivities

The software package Iolite® (Paton et al., 2011) was used to analyze and fit the data. The internal standard was set to be ^{29}Si, with Si present as 23.44 wt% of the mix, which was calculated from the target

50.15% weight percent of SiO_2. Spots visually identified on cracks were removed from the final fit. In cases where the decompression cracks were large, their size was measured with ImageJ and subtracted out from the distance array used for fitting the diffusion profiles.

Our strategy for extracting out diffusivities requires preservation of the initial trace element concentrations on both ends of the diffusion couple. If this is true of the analyte, diffusion profiles can be fit to the following equation:

$$C(x,t) = C_{+\infty} + \frac{C_{-\infty} - C_{+\infty}}{2} * \left(1 - \mathrm{erf}\left(\frac{x - x_0}{2\sqrt{Dt}}\right)\right) \qquad (1)$$

Equation 1 is a 1-dimensional solution to Fick's laws (Crank, 1975) applicable to the boundary conditions used in these experiments as long as the diffusing elements have not yet diffused so far as to overwrite the original $C_{-\infty}$ *(ppm)* and $C_{+\infty}$ *(ppm)* in the diffusion couple. Initial concentrations on each side of the capsule are represented by $C_{-\infty}$ and $C_{+\infty}$. The diffusivity for any particular element is represented by *D* (m^2/s), while *t* (s) is the duration of experiments. Accounting for position in the diffusion couple, *x (m)* is an array from positive to negative taking into account the distance between each of the laser spots. The variable x_0 is the location of the Boltzmann-Matano interface and is limited to one location by the physical realness of mass balance. The concentration at a specific spot on a specific sample is *C(x,t),* a value known from the LA-ICP-MS work. The setup of the experiment constrains $C_{-\infty}$, $C_{+\infty}$, and *t*, while *D* is unknown and the independent variable.

Diffusion profiles were fit using the Global Fit module in the Igor Pro environment. With this module, the profiles for several element analyzed by LA-ICP-MS from a single experimental charge can be fit at the same time. The global fitting procedure allowed $C_{-\infty}$, $C_{+\infty}$, and *D* to vary for each individual element in a fit, whereas the interface location, x_0, is kept fixed for all elements in the fit. Most elements' diffusivities were recovered from this global fitting procedure. Later, other elements, particularly those that did not often have good profiles or appeared to be close to diffusing beyond experiment boundary conditions (e.g. Zn, Co, Mn, Sc and P), would be fit individually or from a secondary LA-ICP-MS session's dataset if that was available. If the data for these individual fits was from the same analytical session, then the same x_o retrieved from the global fit for that session was used for that particular element. For all fits, global and individual, a weighting wave of one standard deviation (1 S.D.) on the concentration data was provided to the Igor Pro fitting routines.

2.7 Mapping

To better understand mass transport in our samples, laser ablation mapping was conducted on the 80 minute MMO experiment. The scan speed used was 20 μm/s with 35 μm square lines that ran the width of the sample. The square lines were cloned over the whole sample to be directly adjacent with no intervening gaps. All other settings were the same as in section 2.6. The mass spectrometer data was imported into Iolite and integrations selected by using the Laser Log file. After data reduction, the Iolite CellSpace (Paul et al., 2012) module was used to overlay the compositional data onto a mosaic image from the laser and colorize by total ppm level.

3. Results

3.1 Documentation of Buffer Material and Example Element Profiles

Figure 2 shows electron backscatter images of the buffering phases in each MMO and RRO experiment. Experiments done in Mo capsules or using the Ru-RuO_2 buffer require confirmation to make sure both phases participating in the buffering reaction are present. For Mo capsules, this means checking that both Mo and MoO_2 are present and chemically communicating with the melt, ensuring an fO_2 equivalent to MMO. When using the Ru-RuO_2 buffering mix, this means confirming that the buffer material of Ru-RuO_2 is still present and has not fully reduced to Ru by the end of the experiment. The two 90 second

experimentsprovide insight on how buffering phases are operating in the experiments from the start. Buffering phases in each experiment from the time series were analyzed by EDS to determine if they were oxidized or native metal.

Patinas that formed in the MMO samples can be seen on the right side of each MMO image. All MMO experiments have this patina which was identified with EDS to be an oxidized Mo phase. The presence of the patina in the 90 second MMO experiment shows that these experiments are buffered to MMO from the at least 1/10 the time of the shortest experiment (20 minutes) used to recover diffusivity. Crystals were present, near the patina and suspended in the silicate glasses of the MMO experiments. These crystals can be seen in MMO images of Figure 2 and when analyzed via EDS return a metallic Mo signature. The presence of both the patina and Mo crystal together suggests the glass is chemically communicating with both native Mo and the oxidized Mo and correctly buffered to MMO. A calcium molybdate phase was also documented by WDS with the electron microprobe connected with the patina in the 20 minute MMO experiment. While not exhaustively searched for, this phase was not observed in any other sample or found again on the 20 minute experiment in the SEM.

For the RRO experiments shown in **Figure 2**, the buffering RRO mixture was examined with backscatter electron microscopy and EDS. For all experiments, both Ru and RuO_2 phases were still present and had not been entirely converted to a single phase of Ru. While there were cases where a reduced wave of Ru was starting to surround the buffer mixture, locations where both Ru and RuO_2 were both in chemical contact with the melt were always found. The 90 second RRO experiment may not have had enough time to fully melt as evidence by the bright and dark phases where just the glass phase should be. There is also some evidence for this in the 20 minute RRO experiment as well. The solid regions that are extremely bright in backscatter represent the Pt-Ru capsules, and in one or two cases pieces of the capsule can be seen in the melt itself (e.g. the 20 and 80 minute RRO experiment)

Experiments done in graphite capsules are taken to be buffered, accepting that the relationship established by Ulmer and Luth (1991) is broadly applicable to our experiments. There is no need to establish the presence of buffering phases for the graphite capsule experiments.

Now that we have established fO_2-buffered conditions, we turn our attention to the diffusion profiles. **Figure 3** shows example profiles of V, Mn, Eu, and W across the oxygen fugacities studied in the 40 minute experiments, all of which have well-formed diffusion profiles. **Fig 3 (a, b)** shows V and Mn across each fO_2 representing profiles from the transition elements while **fig 3 (,c,d)** shows profiles for Eu and W representing the REEs and High Field Strength Elements (HFSEs) repspectively Generally, profiles of the REE and HFSEs were not problematic to fit. The transition elements, except V, were harder to fit. In some cases, these elements presented profiles that appeared to have violated our boundary conditions. For elements such as Cu and Ni, all profiles were poor, so their diffusivity was probably faster than could be accurately measured by these experiments. Many other transition elements, were too fast by the nature of their diffusivities to be properly captured with length scale of the capsule for some (e.g. Zn, Co, and Mn in the 80 minute graphite or 80 minute RRO experiments) of the longer experiments.

For the purpose of further studying the experiments and checking on the contribution of convection to experiments, the 80 MMO-buffered minute experiment was mapped via LA-ICP-MS. Select compositional maps are shown in **Figure 4.** These maps show the region of high-trace elements at the bottom of the capsule, the interface between the two packed powders and the low-trace element region at the top. No overturn of material is seen in the 80 minute MMO map which is taken to mean that convective overturn is not occurring. These maps also enable an enhanced method of extracting diffusivities from the sample. By taking the average of the concentration for each line, well-formed diffusion profiles can sometimes be generated for elements that did not present a good diffusion profile when analyzed in spot mode. **Figure 4(c)** shows and analysis of P in spot mode while **Figure 4(d)** shows the average of each of these lines extending from one edge of the capsule to the other. When fit, 4(d) returned a P diffusivity of $(6.55\pm0.55) \times 10^{-12}$ m^2/s. We now evaluate diffusivities for a range of elements conducted at the same fO_2 for different durations. Figures for the diffusivities recovered at fO_2 and for each duration in the time series can be found in the SOM (**Figs. S1, S2, & S3; SOM**).

3.2 MMO-buffered Experiments (FMQ-3.1), Reducing fO_2

Recovered element diffusivities of MMO-buffered experiments are generally consistent with the elemental diffusivities recovered from the other MMO experiments run for different durations, within 3 S.E. This helps to establish the conditions for the experiments did not change much throughout the time series. Exceptions for certain elements would be the diffusivities of W and Ta for the 80 minute and 40 minute MMO datasets, Ce when the 80 and 20 minute datasets are compared or Co when compared in the 20 and 40 minute datasets as well as the 20 and 80 minute datasets. A few elements deserve extra discussion. Scandium becomes slower as the time series progresses with a diffusivity of $(1.5\pm0.27)\times10^{-11}$ m^2/s in the 20 minute MMO experiment and then a diffusivity of $(7.2\pm1.9)\times10^{-12}$ m^2/s and $(5.5\pm1.8)\times10^{-12}$ m^2/s in the 40 and 80 minute experiments. The best formed diffusion profile for Sc is from the 20 minute run since the 40 and 80 minute experiments both slope up on the left hand side making these profiles harder to interpret than a normal diffusion profile. Incidentally, the fit for Sc from the 80 minute map returns a Sc diffusivity of $(8.3\pm0.95)\times10^{-12}$ m^2/s. Recovered Zn diffusivities from the MMO experiment varies with the 20 minute D at $(4.4\pm0.61)\times10^{-11}$ m^2/s, the 40 minute at $(8.1\pm0.92)\times10^{-11}$ m^2/s and the 80 minute diffusivity from the mapped sample at $(4.0\pm0.44)\times10^{-11}$ m^2/s. The 20 minute experiment exhibits the best profile for the recovery of Zn diffusion. While the 40 minute Zn presented a better spot profile than the 80 minute, there were only a few points to fit a $C_{+\infty}$ to on the right, which possibly interferes with the accuracy of the recovered Zn diffusivity. So the Zn diffusivities recovered from the 40 minute MMO experiments may not be accurate. For Mo in the MMO experiments, only the 40 minute experiment represented a good diffusion profile able to be fit. Analysis of Mo in the 20 minute experiment which presented an otherwise well-formed profile appears to have struck a crystal or bleb in the middle of the diffusion profile. The 80 minute experiment did not present a well-formed profile which is unsurprising since in-diffusion of Mo from the capsule into the melt is likely playing a role here. The best fits in MMO for P, Cr and Zn come from the 80 minute experimental MMO map.

3.3 Graphite Experiments (FMQ-1.2), Intermediate fO_2

Graphite capsule experiments show diffusivities that are fully consistent with each other for the 20 and 40 minute experiments. However the 80 minute experiments show diffusivities slower for every element but are all within 3 S.E. Only Sc when the 80 and 20 minute experiments are compared is outside a 3 S.E. range. While Zn, Co and Mn, diffusion profiles were fit for 20 and 40 minutes experiments, the 80 minute experiment did not yield recoverable $C_{+\infty}$ and $C_{-\infty}$, and thus violated our boundary condition. We did not recover a P profile for the 20 minute or 80 minute graphite experiment so the best fit for P comes from the 40 minute graphite experiment.

3.4 RRO Experiments (FMQ+6), Oxidizing fO_2

Experiments buffered at the RRO equilibrium generally overlap between the 3 S.E. of the fit diffusivity at the 20, 40 and 80 minute experiments. The most notable thing for this time series is that the 20 minute REE diffusivities are generally faster than the 40 and 80 minute diffusivity, but excepting Ce and the transition elements, Co and Mn, there is overlap within 3 S.E. between the diffusivities from the the 20, 40 and 80 minute experiments.

3.5 Complications during Element Fitting Routines across fO_2s

The hardest to fit elements were Cu, Ni, Cr, Sc, and P. In most cases these elements were not included in global fit and were instead fit individually later. Some profiles of Cu and Ni were generated but no diffusivities were recovered for these elements. Copper was not analyzed for every experiment but for every analytical session it was included in, the element never produced a good diffusion profile. The same is also true for Ni. Therefore we report no diffusivity data for Cu or Ni from any of the experiments.

Chromium did not present well-formed diffusion profiles when compared to many of the other elements in the MMO spot analyses but did present a good profile when mapped giving a diffusivity of $(3.3\pm0.56)\times10^{-11}$ m^2/s. The 20 minute graphite experiment did form a Cr profile but did not have many points far from the interface on the right or left side. The 40 minute profile of Cr was marginally better with a few more data points far from the diffusion interface. In the 80 minute graphite experiment Cr appears to have diffused out the left hand side. The recovered diffusivities for Cr in graphite capsule experiments were $(4.2\pm2.2)\times10^{-11}$ m^2/s and $(1.7\pm0.6)\times10^{-11}$ m^2/s in the 20 and 40 minute experiment respectively. The Cr profile in the 20 minute RRO experiment suffers from a large slope up away from from the diffusion profile on the left side and slope going down and away on the right of the interface. It is uncertain what causes this pattern for Cr but it does mean that this profile does not satisfy our boundary conditions. The 40 minute RRO Cr fit was better but still required masking of datapoints on the $C_{+\infty}$ side to generate a proper diffusion couple. For the 80 minute RRO experiment, as a test, ^{52}Cr was analyzed instead of ^{53}Cr, however a well-formed diffusion profile was still not produced. In several experiments, Sc presented fairly good diffusion profiles. However this is complicated by the recovered Sc diffusivities having a wide range throughout the 20, 40 and 80 minute time series at all oxygen fugacities. The best fits for P were at RRO, where it was possible to average the 20, 40 and 80 minute RRO experiments to get $(4.8\pm2.1)\times10^{-12}$ m^2/s. For the graphite experiments, only the P from the 40 minute experiment was able to be fit, returning $(7.0\pm7.7)\times10^{-12}$ m^2/s and even so this profile still required masking.

3.6 Summary of Average Diffusivities for All fO_2s

For each fO_2, the changes across all elements for diffusivity are summarized by the recovered preferred diffusivities in **Table 4**. Errors in **Table 4** are the one sigma errors on the original 20, 40 and 80 minute diffusivities propagated through the averaging process. Elements that could not be fit for the entire time series use diffusivities only from the time series experiments that could be fit, or may use alternate diffusivities retrieved from the mapped MMO experiment.

Figure 5 presents diffusivities from Table 4 graphically. General groupings are apparent for different categories of elements. Elements like W, Ta, Nb, Mo, referred to as the HFSEs, have diffusivities that can be grouped together and are lower in magnitude than those of REEs. The REE elements are faster, sometimes more than twice as much compared to HFSEs for each fO_2. Transition elements like Zn, Co, Mn, and Cr diffuse much faster than the REEs or elements like Mo and W. So much so, that diffusivities for some of the transition elements in **Figure 5** are only averaged from the 20 and 40 minute experiments in their time series. The transition elements are significantly faster than the other elements studied here. Even so, the diffusivities are still in a similar order of magnitude as those of the other elements.

Notably, the diffusivity of V is more in-line with those of the REEs than with transition elements. The diffusivity of Sc is more similar to that of HFSEs than it is to the diffusivity of other transition elements. Although, this is complicated by the diffusivity recovered from Sc profiles having large variations across the time series experiments. Elements diffused the slowest in graphite capsule experiments. The diffusivities of all studied elements – both redox-sensitive and univalent – are changing as fO_2 is varied. The HFSEs are faster at either the reducing (MMO; FMQ-3.1) or oxidizing (RRO; FMQ+6). ends of the spectrum. This is true for REEs (excluding Eu which is fastest in MMO as well), transition elements and the rest. Experiments conducted in the graphite capsules yielded the slowest diffusivities than other fO_2s while in the oxidizing case of RRO they diffused fastest. Note that these overall slower diffusivities do not change the magnitude of element-element fractionations, reviewed in section 3.7.

3.7 Element-Element Fractionations with Changes in fO_2.

3.7.1 Rare Earth Fractionation and the Eu Anomaly

The non redox-sensitive REEs show little fractionation from each other, a point further made by **Figure S4** in the supplemental. Overall this lack of fractionation indicates that the REEs in our experiments

did not experience any significant starting fractionation which is useful for cases made herein regarding diffusion and the redox sensitivity of Eu. An interesting feature in the REE patterns, among the three oxygen fugacities, is presented by Eu. In the MMO case, Eu can be seen in **Figure 5** to have a much higher diffusivity than the other rare earth elements at MMO. In fact, the diffusivity of Eu in the MMO case is ~80% faster than the averaged diffusivity of Sm and Gd. Previous work (e.g. Koepke and Behrens, 2001) has used Sr diffusivity as a stand-in for the diffusivity of Eu^{2+} and the average diffusivity of Sm and Gd as a proxy for Eu^{3+}. This Eu signature is also present in the case of the graphite capsule experiments. There the diffusivity is 44% faster than the averaged diffusivity of Sm and Gd. Finally at an fO_2 RRO, the diffusivity of Eu becomes similar to those of on the other REEs. This indicates that Eu^{2+} was present in the experiments with reducing conditions whereas the element was converted to mostly Eu^{3+} when experiments were done at oxidizing conditions. These results are similar the conclusions of other workers. For example, LaTourrette and Wasserburg (1997) show via absorption spectroscopy that the valence of Eu shifts from Eu^{3+} to $Eu^{2.5+}$ as fO_2 was changed from that of air to Fe-FeO (IW). In their experiments, they also state that the diffusivity of Eu was similar to that of Nd in air, while 42% faster at Fe-FeO which is similar to the graphite-buffered result found here but not as extensive as our MMO (~IW) result. Their experiments were conducted at 1 atm and used a higher temperature range, 1400 ℃ to 1500 ℃.

As Eu^{2+} atoms migrate through the melt, the increased diffusivity of Eu^{2+}, allows them to diffuse farther than Eu^{3+} atoms in the same timeframe. We refer to the signature this appears as when the ratio $Eu/\sqrt{(Sm*Gd)}$, as a proxy for Eu^{2+}/Eu^{3+} is graphed as the Eu anomaly. The magnitude of this anomaly depends on the redox state of the melt and the shift in diffusivities occurring with both the redox sensitive and non-redox sensitive elements. these factors are discussed further in discussion section 4.2 **Figure 6a** shows Sm, Eu, and Gd on the same plot for the 40 minute experiments MMO-buffered experiment while Figure 6b shows the $Eu/\sqrt{(Sm*Gd)}$ ratio for the 40 minute experiments from each oxygen fugacity used in this work. **Figure 6** shows the concentration of Sm, Eu, Gd across a profile taken of the 40 minute MMO experiment as well as a simulated and actual $Eu/\sqrt{(Sm*Gd)}$ for that experiment. These simulation were generated from profiles using the D, $C_{-\infty}$, $C_{+\infty}$, and t of Sm, Eu, and Gd recovered from the fitting procedures outlined in section 2.7. The dotted and solid line simulations are made from 40 minute MMO experiments and 40 minute graphite experiments respectively. Careful examination of **Figure 6** shows that the right hand side of the simulated Eu anomaly levels out at a position just slightly lower than the left-hand side. This is because the simulated Eu anomaly shows Eu, Sm and Gd but with the concentrations on each side recovered by LA-ICP-MS diffusivities As such this subtle distinction in the level of the two sides is a result of a small starting fractionation of the Sm/Eu or Sm/Gd ratio between the high and low trace element ends of the diffusion couples. The curved hill and trough shape in **Figures 6** on the red and blue datasets is caused by the enrichment on one side and depletion on the other vs. the monovalent REEs as Eu^{2+} diffuses. For the dataset from RRO, graphed as connected crosses**,** from the 40 minute experiment done at the oxidizing case of RRO, the Eu anomaly signature vanishes. This suggests that most to nearly all of Eu present has been oxidized into Eu^{3+} and is diffusing at a rate similar to that of the other rare earth elements. Also because of this, there is no simulated Eu anomaly for the RRO case graphed in **Figure 6**. For the graphite case, a Eu anomaly is still present and the magnitude appears to be more subdued than that of MMO in **Figure 6** although it is hard to determine if the magnitude is actually the smaller due to the similarity of the profiles and the size of the error bars. It is still probably indicative of there being some Eu^{2+} present but less than at the more reducing conditions as is further discussed in section 4.1.

3.7.2 Nb/Ta

Other elements ratios present some interesting patterns; Nb/Ta show a small anomaly right at the interface of the diffusion couple (**Fig. 7**). The magnitude of this Nb/Ta anomaly is largest for the most oxidized experiments. **Figure 7** shows the Nb/Ta ratio for the three fO_2-buffered experiments at 40 minutes. A simulated profile in **Figure 7** for the RRO-buffered experiment is shown, which is fit using a Nb/Ta diffusivity ratio of 1.6. This diffusivity ratio was calculated from the actual Nb and Ta diffusivities recovered from the 40 minute RRO buffered experiment.

3.7.3 Other Elemental Patterns and Fractionation between Elements

The transition elements show an interesting pattern across the redox conditions studied and with increasing atomic Z. Examining Mn, Co, Zn in **Fig. 5**, a similar trend can be see for diffusivities of these elements at MMO and RRO, where the diffusivities of these elements decrease with increasing mass. This is not the case for the experiments done in graphite capsules where diffusivities increase with mass for these three elements.

Other elements were explored for redox related fractionations but meaningful statements require certain initial conditions. To ascertain if elements can be fractionated from each other, it is better to have the absence of initial fractionations of the elements between the high and low trace element sides if the diffusion couples. More discussion of certain element ratios can be found in the SOM. Like Sm, Eu, and Gd many of these geochemically interesting element ratios rely on elements that are chemically similar but differ inredox sensitivity. Often they use a non-redox-sensitive element as a proxy (e.g. La and Pr for Ce, Sc for V, etc.). Since we show that there is base change in diffusivities for all elements (including non-redox-senstive element) between fO_2 conditions, this may need to considered for those element ratios.

3.8 Heterogeneities in the starting material

There are also deviations in Fe (e.g. **Table 2**) and some of the trace elements (e.g. Zn) between the three oxygen fugacitites. These variations in compositions still leave the eventual recovered diffusion profiles intact in many cases. Volatilization or alloying with the Pt crucible, an effect that could also be related to redox during the one-bar synthesis could be the cause of the discrepancy. There is also the possibility that certain element groups may be fractionated in the starting material against the other groups of trace elements. While these observations could be the result of the volatilization or interactions with Pt crucible, they might simply be caused by the base mix being contaminated in certain elements.

Since elements were added in basaltic ratios or chondritic abundance relative to each other, our relative element concentrations in our samples will be tolerant to these effects. Also with only intact diffusion profiles being fit, diffusivities recovered are still valid. For element ratios with large starting fractionations, diffusive fractionation would become harder to analyze for but the process does not stop occurring.

4. Discussion:

4.1 Diffusivity of Eu and the Eu anomaly with Oxygen Fugacity

Redox states Eu^{2+} and Eu^{3+} are different in both their charge and their atomic radii, which will influence how these elements interact and complex with the melt. In the case of diffusion, how these elements migrate throughout the melt could be affected. Measuring the result of redox change on Eu is straightforward since the diffusivities of chemically similar but non-redox sensitive elements Sm and Gd can be used to bracket the effect. Our experiments demonstrate that it is possible to generate an Eu anomaly from diffusion alone implying that the diffusivities of Eu^{2+} and Eu^{3+} are different. More reducing conditions should result in increasing the proportion of Eu that is in the Eu^{2+} state. Due to having a lower charge Eu^{2+} should diffuse faster than Eu^{3+}. Overall this will lead to a higher average diffusivity for Eu and thus the magnitude of this Eu anomaly depends on the oxygen fugacity. Notably, in any coordination state, Eu^{2+} will always have a larger ionic radii than Eu^{3+} (Shannon, 1976), although the exact difference between the ionic radii would depend on the coordinations of Eu^{2+} and Eu^{3+} being considered. However the presence of the Eu anomaly in our reducing experiments shows that Eu^{2+}, when present, is diffusing faster than Eu^{3+} despite having a larger ionic radii. Therefore it is probable that the valence change for Eu significantly outweighs the contribution of ionic radii for the diffusive properties of this element. Since mineral growth can be influenced by diffusive supply, there could be consequences for the final chemical composition of

minerals crystallizing from silicate melts, or consequences for the distribution of redox-sensitive elements during magma mingling. In the case of the former, for example, a faster diffusivity for Eu^{2+} compared to Eu^{3+}, could affect the Eu anomaly recorded in plagioclase. Since plagioclase is a major rock-forming mineral that can incorporate Eu^{2+} in the place of Ca in its structure, the resulting Eu anomaly of the melt will be affected. The same mechanism that allows an Eu anomaly to be generated in these experiments will also exist in any case where there is a diffusive boundary (e.g. crystal growth, interface between two magmas mixing in a magma chamber) under reducing conditions. This Eu anomaly leads to a relative enrichment of Eu, compared to Sm and Gd in the low trace element side of the diffusion couple. A relative depletion will form on the other side. In a natural setting, e.g. crystal growth, this will lead to a relative Eu depletion in the melt and relative enrichment of Eu in the up-taking crystal. These physical scenarios are discussed in the section 4.4.

Drake (1975) explored the partitioning of Eu between plagioclase and basaltic melt as a function fO_2 under one atmosphere conditions. The range of oxygen fugacity used corresponded to a ~0.6 more oxidizing than RRO at 1300 °C and to about 1.6 log units more reducing than the IW buffer at 1290 °C. The relative proportions of Eu^{2+} and Eu^{3+} in the melt deduced from that study can be expressed as:

$$\log fO_2 = -4.55(\pm 0.17)\log\frac{Eu^{2+}}{Eu^{3+}} - 10.89(\pm 0.19) \qquad (2)$$

Solving equation 2 for the fO_2 conditions used in the experiments here gives in MMO, an Eu^{2+}/Eu^{3+} ratio equal to 0.76 and graphite capsule experiments, an Eu^{2+}/Eu^{3+} ratio equal to 0.3 showing the decreasing proportion of Eu^{2+} in the melt as conditions become more oxidizing. At RRO, the calculated Eu^{2+}/Eu^{3+} is very low and equal to ~0.01.

If these proportions are taken to be true for the basaltic melts in our experiments, they would allow for direct calculation of the diffusivity of Eu^{2+}. The other basic assumption needed would be that the diffusivity of Eu^{3+} in each experiment can be approximated by taking the average of the diffusivities of Sm and Gd from that experiment. Then the diffusivity of Eu^{2+} could be calculated from equation 3:

$$\overline{D}_{Eu} = \frac{(D_{Eu^{2+}} * A_{Eu^{2+}}) + (D_{Eu^{3+}} * A_{Eu^{3+}})}{(A_{Eu^{2+}} + A_{Eu^{3+}})} \qquad (3)$$

Using the ratios calculated for each fO_2 calculated from eqn. 2, we then find that the diffusivity in the 40 minute experiment of Eu^{2+} at MMO-buffered conditions is $(4.1\pm0.4)\times10^{-11}$ m^2/s, and in graphite capsule experiment, $(3.7\pm1)\times10^{-11}$ m^2/s. Given the decreased abundance of Eu^{2+} under RRO conditions, no Eu^{2+} diffusivities at RRO are presented. Doing the same for the 20 minute experiments, the diffusivity of Eu^{2+} at MMO is $(4.3\pm0.4)\times10^{-11}$ m^2/s, and in the graphite experiment $(3.2\pm0.9)\times10^{-11}$ m^2/s. In the 80 minute MMO case, $(4.6\pm0.4)\times10^{-11}$ m^2/s. Due to large Sm/Gd fractionations in the profile of 80 minute graphite case, that calculation for Eu^{2+} diffusivity is also not presented.

The magnitude of the Eu anomaly observed in our experiments is function of the concentration difference (i.e. $C_{-\infty}$ and $C_{+\infty}$, of the trace elements on one side of the diffusion couple vs. the other side) of the diffusion couples, the initial Eu anomaly on each side, and the oxygen fugacity. The experiments were designed such that the initial Eu anomaly is the same for each side so that an Eu anomaly diffusive fractionation can be studied. Using our calculated diffusivities for Sm, Eu, and Gd, **Figure 8** shows how the magnitude of the anomaly would change with different initial concentration ratios. Both the expected Eu anomaly signature if concentration are no different and if $C_{+\infty}$ is enriched for each trace element 10 times more than in our experiments is shown. Our experimental case has $C_{+\infty}$ enriched about 3.7 to 5 times $C_{-\infty}$ depending on fO_2. Due to the high diffusivity of Eu at MMO, the magnitude of this anomaly grows fastest as the concentration gradient is increased. This is true even though the experiment at this fO_2 only hasa $C_{+\infty}$ that is 3.7 times $C_{-\infty}$ for Sm, Eu and Gd.

4.2 Nb/Ta

As can be seen in **Figure 7**, the Nb/Ta ratio also shows evidence for Nb fractionation from Ta across the plotted diffusion profiles. Some fractionation is expected due to the large difference in the mass

of these elements causing different diffusivities, but the magnitude of this fractionation is larger in RRO-buffered experiments when compared with other fO_2s. These elements may be redox-sensitive and might be reduced to Nb^{2+} and Ta^{3+} at very reducing fO_2 conditions (Cartier et al., 2014) beyond those used in these experiments. However, neither of these elements is thought to have a valence state more oxidized than Nb^{5+} and Ta^{5+}, so a valency change is likely not responsible for the increased fractionation at FMQ+6.

4.3 Other Elements

Some other known redox-sensitive and non-redox sensitive element pairs (e.g. V/Sc) may exhibit trace element fractionation. However due to poor fits on one or the other of their elements in their ratios, not all experiments or element sets are idealized for this. This makes it is difficult to determine if there an effect related specifically to the change in valence on these redox-sensitive elements. Some element ratios (Mn/La) show starting fractionations between the high-trace element and low-trace element side complicating analysis for diffusive trace element fractionation.

4.4 Implications in Natural Systems

Diffusion as a process has implications for mineral growth in planetary magmatic melts. Mineral growth in a magma can be diffusion-limited or depend on a diffusive regime. For example, solutions for the concentration of an element in the boundary layers of growing crystal has been characterized before (Baker, 2008; Smith et al., 1955). In these solutions, there is a dependency on the diffusivity D of the element of interest. This is important for deciding if melt inclusions in crystals are indicative of the parent melt or if they are capturing the signature of diffusive fractionation in the boundary layers of a rapidly growing crystal (Baker, 2008; Watson, 1982).

4.5 Melt Structure Changes and Possibly Redox-Sensitive Elements

On average, between all fO_2s, the diffusivities of the non-redox sensitive elements are the same within a factor of ~2 with some variation depending on the element being compared. Even so, the recovered diffusivities from these different fO_2s are statistically different. In this section, we explore the possibility that melt structure changes occurring with fO_2 could be responsible for this difference. Since diffusivities of both redox sensitive and non-redox-sensitive studied elements are shifting with fO_2, a mechanism affecting all transport process in the melt as fO_2 is varied might exist.

Cations comprising the melt structure are often referred to as network-forming or network–modifying. Network-forming cations are those cations in the melt in tetrahedral coordination (Mysen, 1983) such as Si ions bonded with oxygen in a silicate melt. Network modifiers connect the tetrahedral polymers and units together (Mysen, 1983). A major redox-sensitive element in these experiments is Fe which has redox states of Fe^{o}, Fe^{2+}, and Fe^{3+}. In terrestrial melts as well as the fO_2s explored here, most Fe encountered is in either the 2+ or 3+ state. In a melt, Fe^{3+} occurs in tetrahedral coordination (Mysen et al., 1982) Fe^{3+} but can be both a network former and network modifier. For the other redox state, Fe^{2+} is generally a network modifier although Borisov et al. (2015) mentions that both Fe^{2+} and Fe^{3+} occur in tetrahedral coordination and referring to Shannon (1976) have ionic radii of 0.63 and 0.49 Å respectively. The relative proportion Fe^{2+} and Fe^{3+} will change as fO_2 is varied, possibly altering melt structure. Reducing conditions will probably result in less Fe^{3+} available for tetrahedral coordination in the melt. This would lead to decreased melt polymerization and we suspect would result in faster diffusivities. This matches with the observation that diffusivities in the MMO-buffered experiments are faster than those conducted at an intermediate fO_2. Yet it does not explain why experiments conducted at an intermediate fO_2 have the slowest diffusivities or why the presumably highly polymerized RRO-buffered experiments have the fastest diffusivities. Viscosity is another property of melt and has fundamental relations with diffusivity and whether the cations being studied are network modifying or network forming (Mungall, 2002). If the change

in viscosity is caused by a change in fO_2, there could be systematic changes in diffusivity of the elements in the melt. The Eyring equation (e.g., see Appendices of Mungall, 2002) suggests that the viscosity of the melt and the tracer diffusion of elements through the melt are inversely related. The addition of volatiles can have a multitude of effects on the properties of a magma including viscosity. Tracer diffusivities and the chemical diffusivity of an element not affected by multicomponent effects are very similar and analogous to the diffusivities of trace elements in our experiments. (See Mungall, 2002 for further discussion) Behrens and Hahn (2009) looked at the relationship between viscosity and diffusion experimentally and were able to correlate them for two different melt compositions (phonolitic and trachytic) using the diffusivity of Zr. The effect of the volatile CO_2 on the viscosity of a magma is ambiguous with some reporting little to no change (Morizet et al, 2014) and others reporting that the addition of CO_2 will make a magma more viscous (Papale and Polacci, 1999). The effect is related to polymerization in melt caused by CO_2 and is most likely variable for different compositions of melt. Depending on the change in viscosity for our silicate melts, this could provide a possible explanation for why experiments done in the graphite capsules, which should have more dissolved CO_2, have the diffusivities that are moderately slower when compared the diffusivities recovered from experiments conducted at more oxidizing RRO or more reducing MMO buffers. While a possibility for graphite, this does not provide an explanation for the faster diffusion coefficients encountered in the RRO experiments relative to the other two buffers.

Some elements might have valence changes that are not encountered or significant over the redox range explored here. As mentioned before P^{3+} has been proposed as possible state for P (Mallmann and O'Neil, 2009) yet the Mo-MoO_2 (MMO) buffer is probably not reducing enough to make this a dominant species of P for these experiments. Another would be W whose dominant redox is not expected to change over any of the fugacities explored here.

4.6 Comparisons with Other Work

Holycross and Watson, (2016) conducted diffusion experiments in graphite capsules varying temperatures from 1250 to 1500 ℃ and recovered diffusivities for 25 trace elements, 10 of which overlap with trace elements measured in this study. Both of our experiments use very similar major weight percent element compositions. Diffusivities recovered in this work compare favorably with theirs. Diffusivities from our MMO-buffered experiments are nearly identical with the diffusivities from Holycross and Watson (2016) while our preferred diffusivities from our graphite experiments in **Figure 9** average (excluding Sc) about 55% slower.

Magaritz and Hoffman, (1978) studied the diffusion of Eu and Gd in basalts and obsidian using the radioactive tracer method. In basalt they found the diffusivities for the Eu and Gd tracers to be within their own experimental error of each other at 1150 and 1440 ℃. Their diffusivity for Eu (and thus Gd for that work as well) is $(1.4\pm0.4)\times10^{-11}$ m^2/s which is very similar to the range of diffusivities encountered in this work, especially for experiments done in graphite capsules. The experiments of Magaritz and Hoffman, (1978) were done in air which would oxidize Eu. This may be why no difference between the diffusivities of Gd and Eu were observed. **Figure 9** graphs the comparison between the diffusivities recovered in this paper and those of these workers.

Watson et al. (2015) investigated P diffusion in molten basalt over 1250 to 1500 ℃ and 1 GPa, Calculating with the log D_0 and activation energy from that work, the diffusivity of P at 1300 C is $(6.6\pm0.5)\times10^{-12}$ m^2/s which is similar to our preferred diffusivities reported in Table 4 for P, which range from $(4.8\pm2.1)\times10^{-12}$ m^2/s in RRO to $(7.0\pm7.7)\times10^{-12}$ m^2/s in experiments done in graphite capsules. A number of other studies which focus on the diffusion of trace elements in silicate melts are reported in Zhang et al. (2010), however a range of melt compositions is covered not all of which are basaltic. Some like Lowry et al. (1982) are similar in composition but not identical. A comparison with their recovered Sc, Co and Mn diffusivities in Alkali basalt and the diffusivities recovered in this work shows only moderate difference. At 1300 ℃, they report log D_0 and activation energies that can be calculated to give diffusivitiesof $(3.4\pm1.6)\times10^{-11}$ m^2/s and $(3.2\pm1.2)\times10^{-11}$ m^2/s for Mn^{2+} and Co^{2+} respectively and

$(8.3\pm1.3)\times10^{-12}$ for Sc^{3+}. These are slower than our recovered diffusivities for Mn and Co at any fO_2 but similar in order of magnitude to our experiments. Our diffusivities that are nearest to those of Lowry et al. (1982) come from the graphite capsule and are Mn $(4.3\pm0.4)\times10^{-11}$ m^2/s for Mn and $(4.7\pm0.4)\times10^{-11}$ m^2/s for Co. Their Sc diffusivity is also comparable to what we report in table 4 for Sc diffusivity at any fO_2.

5. Summary and Outlook

Oxygen fugacity conditions can have an effect on the diffusivity of elements. Most elements were found to have the slowest diffusivities when the experiments were done in graphite (FMQ-1.2) capsules. Diffusivities were faster at MMO (FMQ-3.1) and fastest at RRO (FMQ+6). Figure 8 shows that increased differences between the starting concentrations can increase the fractionation in the experiment. Over the ranges of fO_2 studied here, Eu is specially affected. At 1300 °C, differences can be seen in the diffusivities of Eu, recorded across the MMO, graphite, RRO fO_2 buffers. Evidence of diffusive fractionation can be seen by plotting Eu/√(Sm*Gd) for the experiment done in graphite capsule or the MMO. Increased fractionation of the Nb/Ta ratio is seen at RRO. Finally, diffusivities of even the non-redox sensitive elements seem broadly affected by fO_2. Higher temperatures could also change the speciation of Eu. If this causes the proportion of Eu^{2+}/Eu^{3+} to increase, then the magnitude of the Eu anomaly will increase along with average diffusivity of total Eu.

There are also small systematic changes in the diffusivities of all elements, even non-redox-sensitive, as fO_2 changes. These may caused be structural changes in the melt that co-occur with the fO_2 changes. Stuructual changes in the melt could help to explain the variation of the diffusivities of the non-redox-sensitive elements at different fO_2 conditions. Diffusion will control the supply of elements to a mineral growing in a magma. If fO_2 affects the diffusivities of both redox sensitive and non-redox sensitive elements, then there are ramifications for the processes that depend on these elements. As such fO_2 may be important beyond just determining valence and mineral phase because it may affect magmatic mineral growth.

Overall, changes in diffusivities with fO_2 for both elements sensitive to redox and those non-sensitive may have importantimplications for mineral growth and any process that depends on uptake of these elements.

ACKNOWLEDGMENTS

We would like to extend thanks to Jacobs, NASA Johnson Space Center, NASA ARES and the JETS contract. This work partially supported by EAR-1751903. We are grateful to Loan Le for assistance with fO_2 pre-synthesis steps and SEM. We are also grateful for Brian McIntyre's help on SEM at the University of Rochester as well as Zhan Peng, Eve Berger, and Kent Ross for their help with LA-ICP-MS, SEM, and electron microprobe respectively at JSC. Also thanks are due to Jenny Rapp, Kevin Righter, Kellye Pando, Kathleen Vander Kaaden, Rick Rowland, Yanling Wang, Jacob Buettner, and Wriju Chowdhury. The LA-ICP-MS instrument at the University of Rochester is partially supported by a grant from the Instrumentation and Facilities Program, Division of Earth Sciences, NSF (EAR-1545637).

REFERENCES CITED:

Anders, E., & Grevesse, N. (1989). Abundances of the elements: Meteoritic and solar. *Geochimica et Cosmochimica Acta, 53*(1), 197-214.

Baker, D. R. (2008). The fidelity of melt inclusions as records of melt composition. *Contributions to Mineralogy and Petrology, 156*(3), 377-395.

Barrat, J., Zanda, B., Moynier, F., Bollinger, C., Liorzou, C., & Bayon, G. (2012). Geochemistry of CI chondrites: Major and trace elements, and Cu and Zn Isotopes. *Geochimica et Cosmochimica Acta, 83*, 79-92.

Behrens, H., & Hahn, M. (2009). Trace element diffusion and viscous flow in potassium-rich trachytic and phonolitic melts. *Chemical Geology, 259*(1-2), 63-77.

Bird, J. M., & Weathers, M. S. (1977). Native Iron Occurrences of Disko Island, Greenland. *The Journal of Geology, 85*(3), 359-371.

Bockrath, C. (2004). Fractionation of the Platinum-Group Elements During Mantle Melting. *Science, 305*(5692), 1951-1953.

Borisov, A., Behrens, H., & Holtz, F. (2015). Effects of melt composition on Fe3 /Fe2 in silicate melts: a step to model ferric/ferrous ratio in multicomponent systems. *Contributions to Mineralogy and Petrology, 169*(2).

Burnham, A. D., & Berry, A. J. (2012). An experimental study of trace element partitioning between zircon and melt as a function of oxygen fugacity. *Geochimica et Cosmochimica Acta, 95*, 196-212.

Burnham, A. D., Berry, A. J., Wood, B. J., & Cibin, G. (2012). The oxidation states of niobium and tantalum in mantle melts. *Chemical Geology, 330-331*, 228-232.

Burnham, A., & Berry, A. (2014). The effect of oxygen fugacity, melt composition, temperature and pressure on the oxidation state of cerium in silicate melts. *Chemical Geology, 366*, 52-60.

Carmichael, I.S.E. And Ghiorso, M.S. (1990) The Effect of Oxygen Fugacity on the Redox State of Natural Liquids And Their Crystallizing Phases Reviews in Mineralogy and Geochemistry, Volume 24, Issue 1.Chapter 7, Pg. 191-212.

Cartier, C., Hammouda, T., Boyet, M., Bouhifd, M. A., & Devidal, J. (2014). Redox control of the fractionation of niobium and tantalum during planetary accretion and core formation. *Nature Geoscience, 7*(8), 573-576.

Coons, W. E., & Holloway, J. R. (1979) Cobaltous oxide as a chemical analogue for ferrous iron in experimental petrology: An alternative solution to the iron-loss problem. *American Mineralogist, 64*(9-10), 1097-1106.

Cottrell, E., & Kelley, K. A. (2011). The oxidation state of Fe in MORB glasses and the oxygen fugacity of the upper mantle. *Earth and Planetary Science Letters, 305*(3-4), 270-282.

Crank, J. (2011). *The mathematics of diffusion*. Oxford University Press: Oxford.

Diener, J. F., & Powell, R. (2010). Influence of ferric iron on the stability of mineral assemblages. *Journal of Metamorphic Geology, 28*(6), 599-613.

Drake, M. J. (1975). The oxidation state of europium as an indicator of oxygen fugacity. *Geochimica et Cosmochimica Acta, 39*(1), 55-64.

Duncan A. R., McKay S. M., Stoeser J. W., Lindstrom M. M., Lindstrom D. J., Fruchter J. S. & Goles G. G. (1975) Lunar Polymict Breccia 14321: a compositional study of its principal components, *Geochimica et Cosmochimica Acta, 39*, 247-260.

Elardo, S. M., Draper, D. S., & Shearer, C. K. (2011). Lunar Magma Ocean crystallization revisited: Bulk composition, early cumulate mineralogy, and the source regions of the highlands Mg-suite. *Geochimica et Cosmochimica Acta, 75*(11), 3024-3045.

Evans, K. A., Elburg, M. A., & Kamenetsky, V. S. (2012). Oxidation state of subarc mantle. *Geology, 40*(9), 783-786.

Farges, F., Siewert, R., Ponader, C. W., Brown, G. E., Pichavant, M., & Behrens, H. (2006). Structural Environments Around Molybdenum In Silicate Glasses And Melts. II. Effect Of Temperature, Pressure, H_2O, Halogens And Sulfur. *The Canadian Mineralogist, 44*(3), 755-773.

Gaillard, F., Scaillet, B., Pichavant, M., & Iacono-Marziano, G. (2015). The redox geodynamics linking basalts and their mantle sources through space and time. *Chemical Geology, 418*, 217-233.

Goodrich, C. A., & Bird, J. M. (1985). Formation of Iron-Carbon Alloys in Basaltic Magma at Uivfaq, Disko Island: The Role of Carbon in Mafic Magmas. *The Journal of Geology, 93*(4), 475-492.

Hensen, B. J. (1986). Theoretical phase relations involving cordierite and garnet revisited: the influence of oxygen fugacity on the stability of sapphirine and spinel in the system Mg-Fe-Al-Si-O. *Contributions to Mineralogy and Petrology, 92*(3), 362-367.

Herd, C. D., Borg, L. E., Jones, J. H., & Papike, J. J. (2002). Oxygen fugacity and geochemical variations in the martian basalts: implications for martian basalt petrogenesis and the oxidation state of the upper mantle of Mars. *Geochimica et Cosmochimica Acta, 66*(11), 2025-2036.

Huebner, J., & Sato, M. (1970). The Oxygen Fugacity-Temperature Relationships of Manganese Oxide And Nickel Oxide Buffers. *American Mineralogist, 55*(5-6), 934-952.

Holycross, M. E., & Watson, E. B. (2016). Diffusive fractionation of trace elements in basaltic melt. *Contributions to Mineralogy and Petrology, 171*(10).

Igor Pro (Wavemetrics, Lake Oswego, OR, USA)

Jarosewich, E., Nelen, J., & Norberg, J. A. (1980). Reference Samples for Electron Microprobe Analysis*. *Geostandards and Geoanalytical Research, 4*(1), 43-47.

Koepke, J., & Behrens, H. (2001). Trace element diffusion in andesitic melts: An application of synchrotron X-ray fluorescence analysis. *Geochimica Et Cosmochimica Acta, 65*(9), 1481-1498.

LaTourrette, T. & Wasserburg, G.J. (1997). Self diffusion of europium, neodymium, thorium, and uranium in haplobasaltic melt: The effect of oxygen fugacity and the relationship to melt structure. *Geochimica Et Cosmochimica Acta, 61*(15), 3277.

Lee, C. A., Luffi, P., Roux, V. L., Dasgupta, R., Albaréde, F., & Leeman, W. P. (2010). The redox state of arc mantle using Zn/Fe systematics. *Nature, 468*(7324), 681-685.

Leitzke, F., Fonseca, R., Sprung, P., Mallmann, G., Lagos, M., Michely, L., & Münker, C. (2017). Redox dependent behaviour of molybdenum during magmatic processes in the terrestrial and lunar mantle: Implications for the Mo/W of the bulk silicate Moon. *Earth and Planetary Science Letters, 474*, 503-515.

Li, Z. A., & Lee, C. A. (2004). The constancy of upper mantle fO_2 through time inferred from V/Sc ratios in basalts. *Earth and Planetary Science Letters, 228*(3-4), 483-493.

Linnen, R. L., Pichavant, M., Holtz, F., & Burgess, S. (1995). The effect of on the solubility, diffusion, and speciation of tin in haplogranitic melt at 850 °C and 2 kbar. *Geochimica et Cosmochimica Acta, 59*(8), 1579-1588.

Lowry, R. K., Henderson, P., & Nolan, J. (1982). Tracer diffusion of some alkali, alkaline-earth and transition element ions in a basaltic and an andesitic melt, and the implications concerning melt structure. *Contributions to Mineralogy and Petrology, 80*(3), 254-261.

Magaritz, M., & Hofmann, A. W. (1978). DIffusion of Eu and Gd in basalt and obsidian. *Geochimica et Cosmochimica Acta, 42*(6), 847-858. doi:10.1016/0016-7037(78)90097-2

Mallmann, G., & O'Neill, H. S. (2009). The Crystal/Melt Partitioning of V during Mantle Melting as a Function of Oxygen Fugacity Compared with some other Elements (Al, P, Ca, Sc, Ti, Cr, Fe, Ga, Y, Zr and Nb). *Journal of Petrology, 50*(9), 1765-1794.

Mccord, T. B., Adams, J. B., & Johnson, T. V. (1970). Asteroid Vesta: Spectral Reflectivity and Compositional Implications. *Science, 168*(3938), 1445-1447.

Morizet, Y., Paris, M., Gaillard, F., & Scaillet, B. (2014). Carbon dioxide in silica-undersaturated melt Part II: Effect of CO 2 on quenched glass structure. *Geochimica Et Cosmochimica Acta, 144*, 202-216.

Mungall, J. E. (2002). Empirical models relating viscosity and tracer diffusion in magmatic silicate melts. *Geochimica et Cosmochimica Acta, 66*(1), 125-143.

Myers, J., & Eugster, H. P. (1983). The system Fe-Si-O: Oxygen buffer calibrations to 1,500K. *Contributions to Mineralogy and Petrology, 82*(1), 75-90.

Mysen, B. O., (1983). The structure of silicate melts. *Ann. Rev. Earth Planet Sci. 11,* 75-97

Mysen, B. O., Virgo, D., & Seifert, F. A. (1982). The structure of silicate melts: Implications for chemical and physical properties of natural magma. *Reviews of Geophysics, 20*(3), 353.

Nakamura, E., & Kushiro, I. (1998). Trace element diffusion in jadeite and diopside melts at high pressures and its geochemical implication. *Geochimica et Cosmochimica Acta, 62*(18), 3151-3160.

O'Neill, H. S., & Nell, J. (1997). Gibbs free energies of formation of RuO_2, IrO_2, and OsO_2: A high-temperature electrochemical and calorimetric study. *Geochimica Et Cosmochimica Acta, 61*(24), 5279-5293.

Oneill, H. S., & Pownceby, M. I. (1993). Thermodynamic data from redox reactions at high temperatures. I. An experimental and theoretical assessment of the electrochemical method using stabilized zirconia

electrolytes, with revised values for the Fe-"FeO", Co-CoO, Ni-NiO and Cu-Cu2O oxygen buffers, and new data for the W-WO2 buffer. *Contributions to Mineralogy and Petrology, 114*(3), 296-314.

O'Neill, H. S., (1986) Mo-MoO_2 (MOM) oxygen buffer and the free energy of formation of MoO_2 *American Mineralogist, 71*, 1007-1010.

Papike, J., Karner, J., & Shearer, C. (2004). Comparative planetary mineralogy: V/(Cr Al) systematics in chromite as an indicator of relative oxygen fugacity. *American Mineralogist, 89*(10), 1557-1560.

Paul, B., Paton, C., Norris, A., Woodhead, J., Hellstrom, J., Hergt, J., and Greig, A., 2012, CellSpace: A module for creating spatially registered laser ablation images within the Iolite freeware environment: *Journal of Analytical Atomic Spectrometry,* v. 27, no. 4, p. 700,

Papale, P., & Polacci, M. (1999). Role of carbon dioxide in the dynamics of magma ascent in explosive eruptions. *Bulletin of Volcanology, 60*(8), 583-594.

Paton, C., Hellstrom, J., Paul, B.,Woodhead, J. and Hergt, J. 2011. "Iolite: Freeware for the visualisation and processing of mass spectrometric data." *Journal of Analytical Atomic Spectrometry*.

Pourmand, A., Dauphas, N., & Ireland, T. J. (2012). A novel extraction chromatography and MC-ICP-MS technique for rapid analysis of REE, Sc and Y: Revising CI-chondrite and Post-Archean Australian Shale (PAAS) abundances. *Chemical Geology, 291*, 38-54.

Pringle, E. A., Savage, P. S., Badro, J., Barrat, J., & Moynier, F. (2013). Redox state during core formation on asteroid 4-Vesta. *Earth and Planetary Science Letters, 373*, 75-82.

Roux, V. L., Lee, C., & Turner, S. (2010). Zn/Fe systematics in mafic and ultramafic systems: Implications for detecting major element heterogeneities in the Earth's mantle. *Geochimica Et Cosmochimica Acta, 74*(9), 2779-2796.

Russell, C. T., Raymond, C. A., Coradini, A., Mcsween, H. Y., Zuber, M. T., Nathues, A., . . . Titus, T. N. (2012). Dawn at Vesta: Testing the Protoplanetary Paradigm. *Science, 336*(6082), 684-686.

Ruzicka, A., Snyder, G. A., & Taylor, L. A. (2001). Comparative geochemistry of basalts from the moon, earth, HED asteroid, and Mars: implications for the origin of the moon. *Geochimica et Cosmochimica Acta, 65*(6), 979-997.

Sato M., Hickling N., & McLane J. (1973) Oxygen fugacity values of Apollo 12, 14, and 15 lunar samples and reduced state of lunar magmas, Proceedings of the 4th Lunar Science Conference, *Geochimica et Cosmochimica Acta, 1*, 1061-1079.

Schreiber, H. D., Lauer, H. V., & Thanyasiri, T. (1980). The redox state of cerium in basaltic magmas: An experimental study of iron-cerium interactions in silicate melts. *Geochimica Et Cosmochimica Acta, 44*(10), 1599-1612.

Siebert, J., Corgne, A., & Ryerson, F. J. (2011). Systematics of metal–silicate partitioning for many siderophile elements applied to Earth's core formation. *Geochimica Et Cosmochimica Acta, 75*(6), 1451-1489.

Shannon, R. D. (1976). Revised effective ionic radii and systematic studies of interatomic distances in halides and chalcogenides. *Acta Crystallographica Section A, 32*(5), 751-767.

Shearer, C., Papike, J., & Karner, J. (2006). Pyroxene europium valence oxybarometer: Effects of pyroxene composition, melt composition, and crystallization kinetics. *American Mineralogist, 91*(10), 1565-1573.

Steenstra, E., Knibbe, J., Rai, N., & Westrenen, W. V. (2016). Constraints on core formation in Vesta from metal–silicate partitioning of siderophile elements. *Geochimica et Cosmochimica Acta, 177*, 48-61.

Smith, V.G., Tiller, W. A., & Rutter, J. W. (1955). A mathematical analysis of solute redistribution during solidification, *Canadian Journal of Physics, 33*, 723-744.

Thibault, Y. & Walter M. J. (1995). The influence of pressure and temperature on the metal-silicate partition coefficients of nickel and cobalt in a model C1 chondrite and implications for metal segregation in a deep magma ocean. *Geochimica Et Cosmochimica Acta, 59*(5), 991-1002.

Trail, D., Watson, E.B., and Tailby, N.D. (2011) The oxidation state of Hadean magmas and implications for early Earth's atmosphere. *Nature*, 480, 79-82.

Trail, D., Watson, E. B., & Tailby, N. D. (2012). Ce and Eu anomalies in zircon as proxies for the oxidation state of magmas. *Geochimica et Cosmochimica Acta, 97*, 70-87.

Ulmer, P., and Luth, R.W., (1991) "The Graphite-COH Fluid Equilibrium in P, T, fO2 Space."Contr Mineral Petrol Contributions to Mineralogy and Petrology 106(3) 265-72.

Wade, J., Wood, B. J., & Norris, C. A. (2013). The oxidation state of tungsten in silicate melt at high pressures and temperatures. *Chemical Geology, 335*, 189-193.

Watson, E. B., Sneeringer, M. A., & Ross, A. (1982). Diffusion of dissolved carbonate in magmas: Experimental results and applications. *Earth and Planetary Science Letters, 61*(2), 346-358.

Watson, E. B., & Müller, T. (2009). Non-equilibrium isotopic and elemental fractionation during diffusion-controlled crystal growth under static and dynamic conditions. *Chemical Geology, 267*(3-4), 111-124.

Watson, E. B., Cherniak, D., & Holycross, M. (2015). Diffusion of phosphorus in olivine and molten basalt. *American Mineralogist, 100*(10), 2053-2065.

Wilke, M., & Behrens, H. (1999). The dependence of the partitioning of iron and europium between plagioclase and hydrous tonalitic melt on oxygen fugacity. *Contributions to Mineralogy and Petrology, 137*(1-2), 102-114.

Zhang, Y., Ni, H., & Chen, Y. (2010). Diffusion Data in Silicate Melts. *Reviews in Mineralogy and Geochemistry, 72*(1), 311-408.

Table 1:

		oxygen fugacity		
Element	RRO (FMQ+6.0 or IW+9.45)	Graphite Buffer (FMQ-1.2 or IW+2.3)	MMO (FMQ-3.1 or IW+0.4)	Source
P	P^{5+}	P^{5+}	P^{5+}	Mallmann and O'Neill, 2009
V	V^{5+}	V^{4+}	V^{3+}	Papike et al., 2004
Mn	Mixed Mn^{3+}, Mn^{2+}	Mn^{2+}	Mn^{2+}	Huebner and Sato, 1970
Fe	Fe^{3+}	Fe^{2+}	Fe^{2+}	Papike et al., 2004
Co	Co^{2+}	Co^{2+}	Co^{2+}	Thibault et al., 1995, Coons and Holloway, 1979
Zn	Zn^{2+}	Zn^{2+}	Zn^{2+}	Roux et al., 2010, Siebert et al., 2011
Cr	Cr^{3+}	Cr^{3+}	Cr^{3+}	Papike et al., 2004
Nb	Nb^{5+}	Nb^{5+}	Nb^{5+}	Mallmann and O'Neill, 2009
Mo	Mo^{6+}	Mo^{6+}	Mo^{6+}	Leitzke et al., 2017; Farges et al., 2006
Ce	Ce^{3+}	Ce^{3+}	Ce^{3+}	Schreiber et al., 1980; Burnham and Berry, 2014
Eu	Eu^{3+}	Eu^{3+}	Eu^{3+}	Papike et al., 2004
Ta	Ta^{5+}*	Ta^{5+}	Ta^{5+}	Burnham et al., 2012
W	W^{6+}	W^{6+}	W^{6+}	Wade et al., 2013

*** likely dominant species, not fully calibrated over fO_2 range**

Table 2:

Target and Actual Major Weight Percent Elements

1 atm synthesis fO_2 target		FMQ-3.1	FMQ-1.2	100% CO_2
Used for:		MMO Experiments	Graphite Experiments	RRO Experiments
Elements:	Target (wt %)			
SiO_2	50.15	54.14	51.32	50.21
MgO	6.86	7.25	6.98	6.53
Al_2O_3	16.04	15.14	14.95	16.00
FeO	10.74	7.79	11.15	10.96
CaO	9.65	10.3	9.94	9.56
Na_2O	2.97	2.97	2.95	3.42
K_2O	1.12	0.6	0.589	0.626
TiO_2	1.88	1.95	1.99	1.85
MnO	Trace	0.049	0.083	0.026

Table 3:

Target Trace Elements Concentrations and Enrichments

Element or Oxide	Target (wt%) of components in trace mix	Added As
K_2O	1.48	K_2CO_3
P_2O_5	1.48	$CaHPO_4 \cdot 2H_2O$
Sc	0.09	Sc_2O_3
TiO_2	22.2	TiO_2
V	0.776	V_2O_5
Cr_2O_3	1.48	Cr_2O_3
MnO	17.8	MnO_2
Co	7.69	CoO
Ni	0.766	NiO
Cu	1.88	Cu_2O
Zn	4.49	ZnO
Nb*	4.28	Nb_2O_5
Mo*	13.7	MoO_2
La*	3.48	La_2O_3
Ce*	8.89	CeO_2
Pr*	1.35	Pr_6O_{11}
Sm*	2.30	Sm_2O_3
Eu*	0.887	Eu_2O_3
Gd*	3.10	Gd_2O_3
Ta*	0.219	Ta_2O_5
W*	1.63	WO_2

Table 3:

* indicates an element enriched 1000 times chondritic abundance. The target wt % column already takes this enrichment into account.

Sources: Elardo et al. (2011): Lunar Primitive Upper Mantle, ppm, Barrat et al (2012): Orgueil, Ruzicka et al. (2000) Low Ti-Mare Basalt, Anders and Grevasse (1989), Pourmand et al. (2012)

Table 4:

Average Diffusivities of Elements with Well-formed Profiles from Time Series Experiments (in m^2/s)

	RRO	1 S.E.	Graphite	1 S.E.	MMO	1 S.E.
P	4.8E-12	±2.1E-12	7.0E-12[A]	±7.7E-12	4.3E-12[A]	±3.3E-12
Sc	1.1E-11	±2.4E-12	5.9E-12	±2.6E-12	9.3E-12	±1.3E-12
V	1.6E-11	±7.1E-13	1.0E-11	±8.8E-13	1.5E-11	±5.2E-13
Cr	N/A	N/A	2.9E-11*	1.2E-11	3.3E-11[C]	±5.6E-12
Mn	1.1E-10*	±3.8E-12	4.3E-11*	±4.4E-12	7.2E-11	±2.3E-12
Co	9.1E-11*	±1.8E-12	4.7E-11*	±3.5E-12	6.6E-11	±1.7E-12
Zn	8.0E-11[B]	±3.3E-12	5.5E-11*	±4.7E-12	5.1E-11[B]	±4.5E-12
Nb	1.3E-11	±3.4E-13	5.8E-12	±3.3E-13	9.1E-12	±2.4E-13
Mo	1.2E-11	±3.3E-13	6.3E-12	±3.3E-13	7.6E-12[A]	±5.8E-13
La	2.3E-11	±5.0E-13	9.7E-12	±4.8E-13	1.6E-11	±4.0E-13
Ce	2.5E-11	±4.8E-13	1.0E-11	±4.8E-13	1.7E-11	±4.2E-13
Pr	2.5E-11	±5.1E-13	1.0E-11	±5.4E-13	1.6E-11	±4.0E-13
Sm	2.4E-11	±6.4E-13	1.0E-11	±6.5E-13	1.6E-11	±5.2E-13
Eu	2.4E-11	±6.0E-13	1.4E-11	±8.4E-13	2.8E-11	±7.6E-13
Eu^{2+}	4.3E-11	±0.2E-12	3.5E-11*	±0.7E-12	N/A	N/A
Gd	2.2E-11	±5.7E-13	9.6E-12	±5.8E-13	1.5E-11	±4.3E-13
Ta	9.0E-12	±3.2E-13	4.4E-12	±3.8E-13	7.1E-12	±3.1E-13
W	1.1E-11	±3.2E-13	5.2E-12	±3.5E-13	8E-12	±2.8E-13

Table 4: Excepting diffusivities tagged with *, [A] , [B] or [C], all diffusivities here are full averages of the time series experiments.

* Average of only 20 and 40 minute experiments.

[A]Diffusivity from only the 40 minute experiment.

[B]Indicates possible inaccuracy due to inconsistency in diffusivities from time series.

[C]Diffusivity shown from 80 minute MMO-buffered mapped experiment rather than time series.

Figures:

Figure 1:

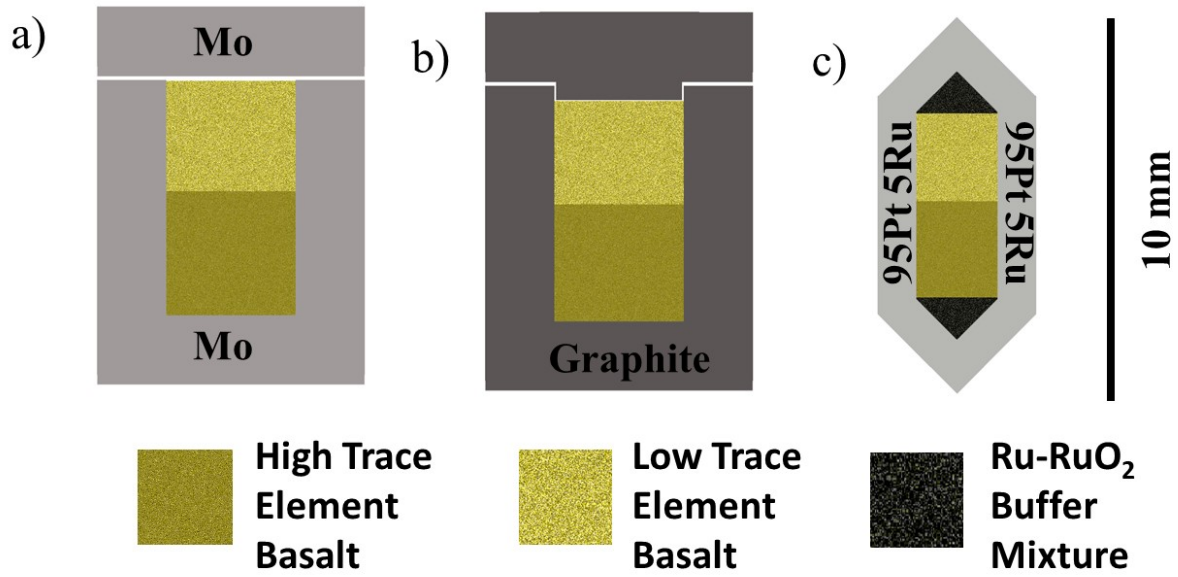

Fig. 1: Experimental capsule designs used at the three oxygen fugacities with showing the a) MMO design b) graphite design and c) the RRO design.

Figure 2:

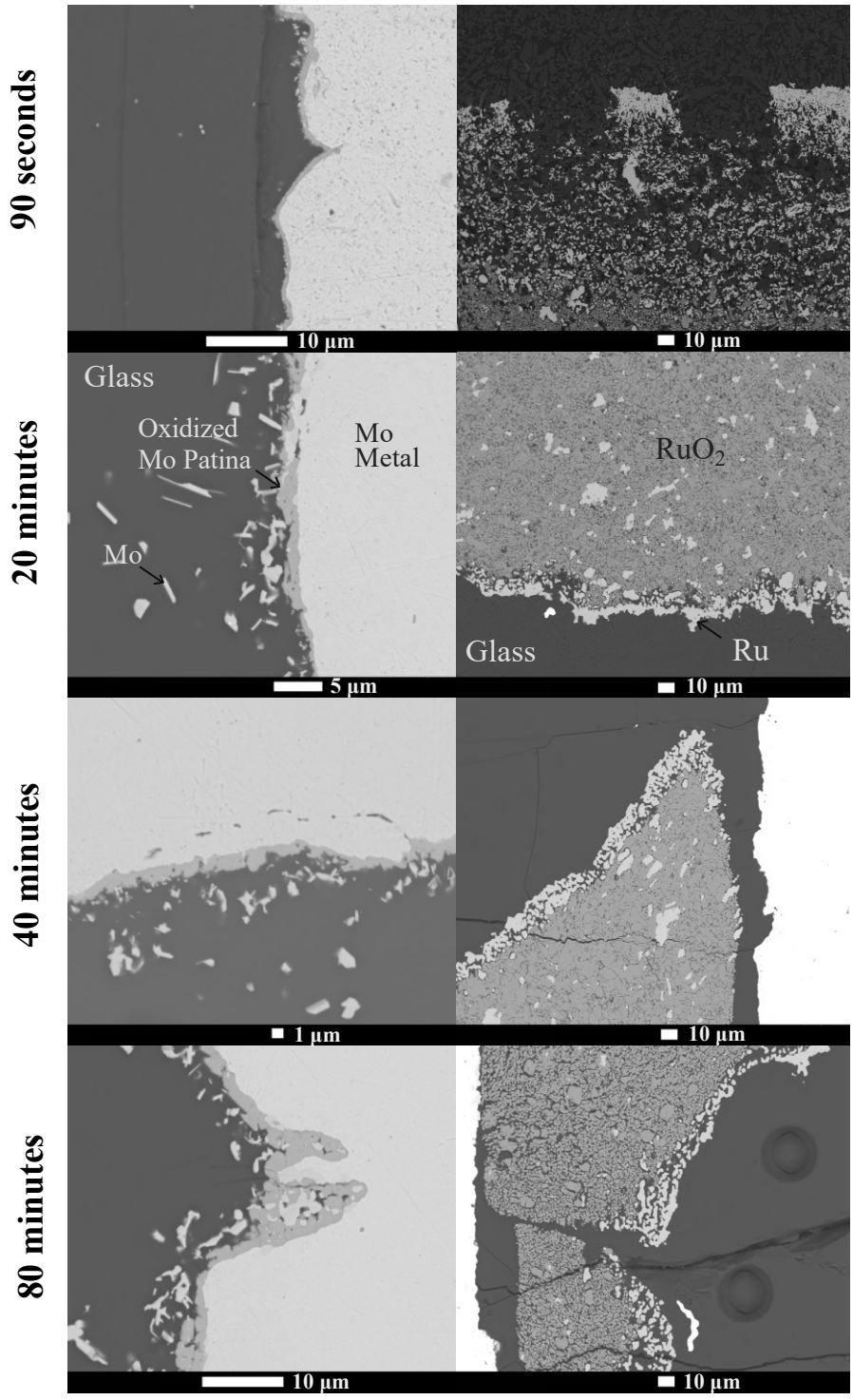

Fig. 2: Electron backscatter images of the buffering phases in MMO- (left) and RRO-buffered (right) samples. The dark region in each of the images corresponds to the quenched melt and is labeled glass in the 20 minute MMO and RRO images. Each of the images in the MMO column show an oxidized patina in between the glass and Mo crystals suspended in the melt can also be seen. A Mo-oxide patina can be

seen on the edge of the capsule walls in contact with the quenched glass, which is observed even after 90 seconds. The RRO-buffered samples show the buffering mixture in contact with the glass. In all experiments both phases participating the fO2 buffering reaction were documented at experiment completion.

Figure 3:

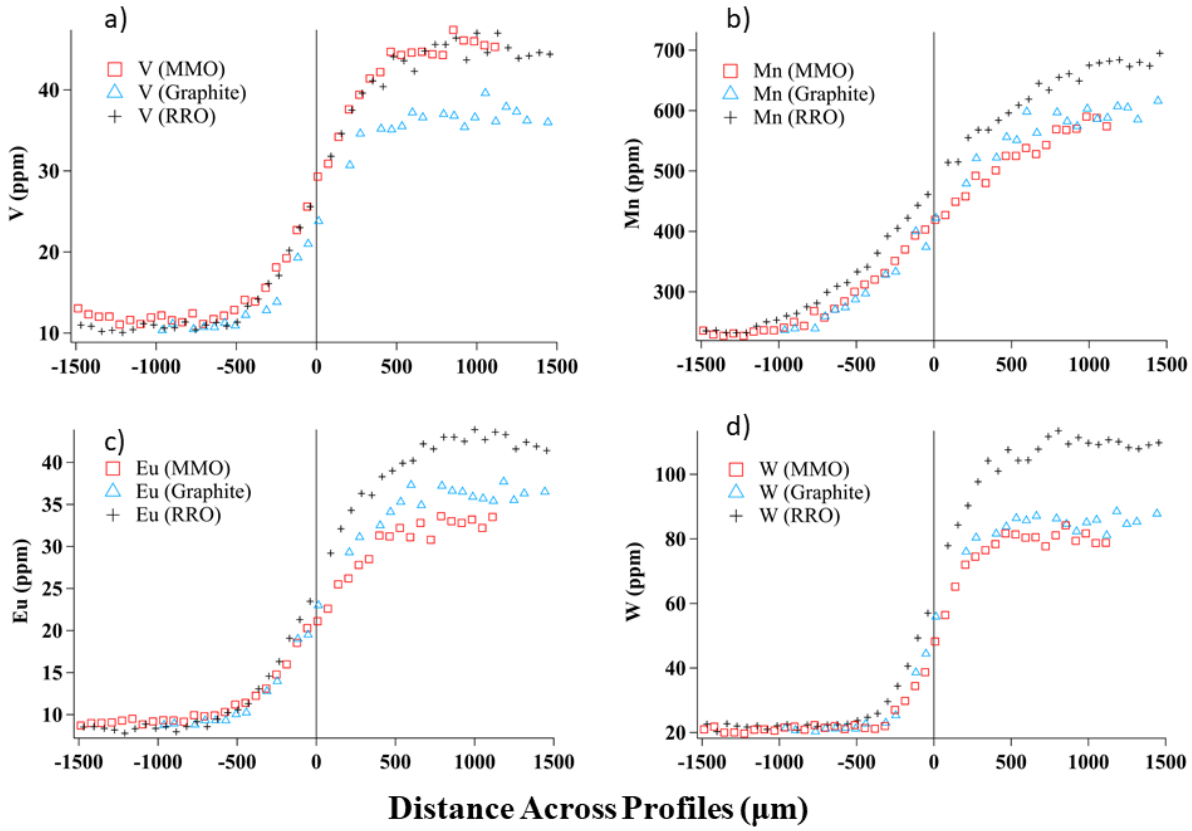

Fig. 3: Diffusion profiles for V, Mn, Eu, and W across all three oxygen fugacitites used in this study for the 40 minute experiments. Each graph contains three lines, one for each fO_2 buffer. Profiles are example profiles taken from the different categories of elements in the experiments with transition elements V and Mn, REE Eu, and HFSEs W.

Figure 4:

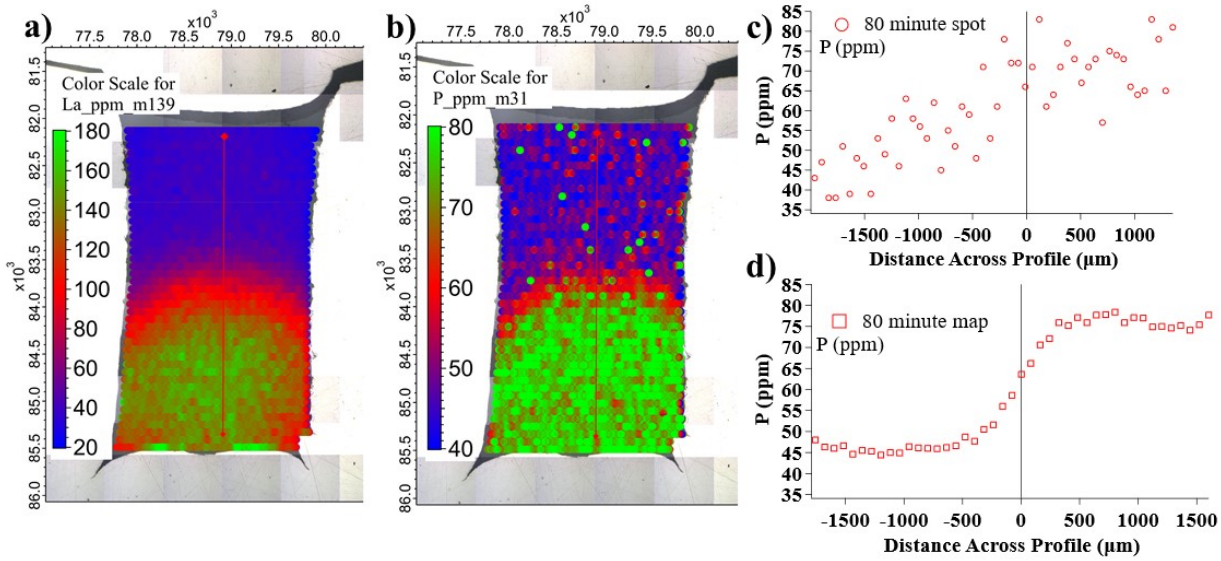

Figure 4: (a,b) An Iolite ® CellSpace LA-ICP-MS map of La and P concentrations from a mapped sample (80 minutes, 1300 °C, 1 GPa, MMO-buffered). The low trace element and high-trace element interface can be identified. (c) A spot mode analysis of P from the same experiment **(d)** A P diffusion profile generated by averaging each line from 4b into an individual point.

Figure 5:

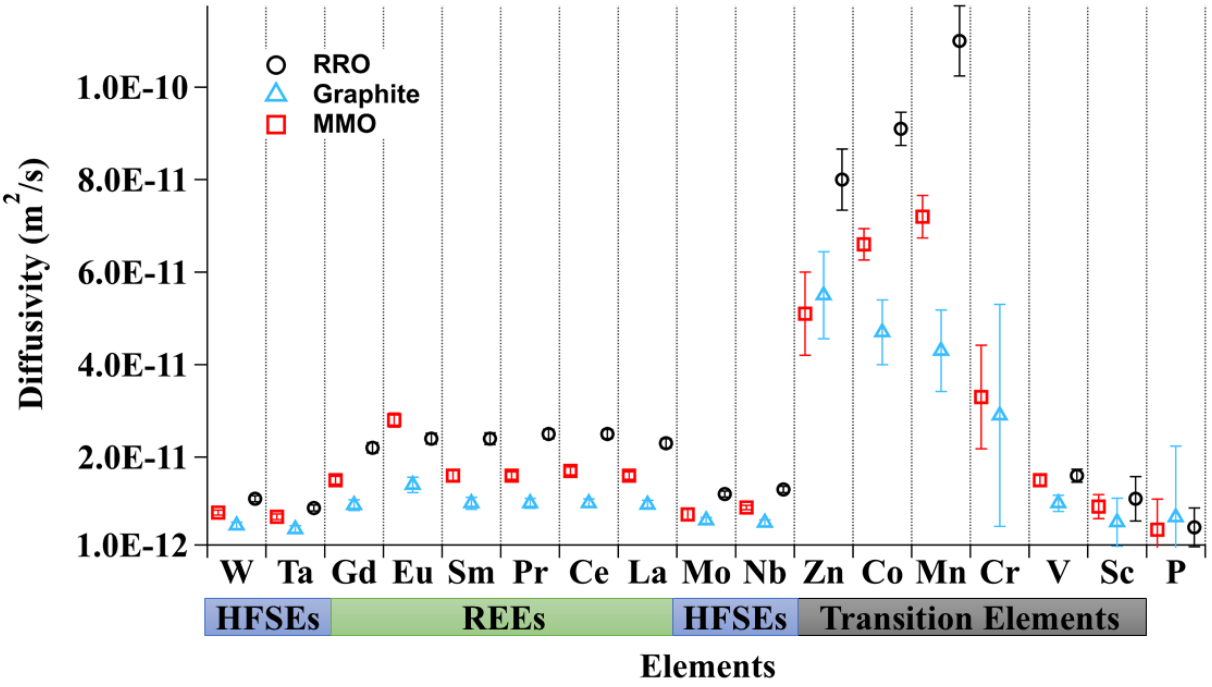

Fig. 5: Our preferred diffusivities (from Table 4) of elements from the MMO- buffered, graphite - buffered and RRO-buffered experiments. The diffusivities calculated for RRO-buffered experiments are the fastest. Error bars are 2 S.E.. If error bars are not visible, then they are smaller than the symbol size.

Figure 6:

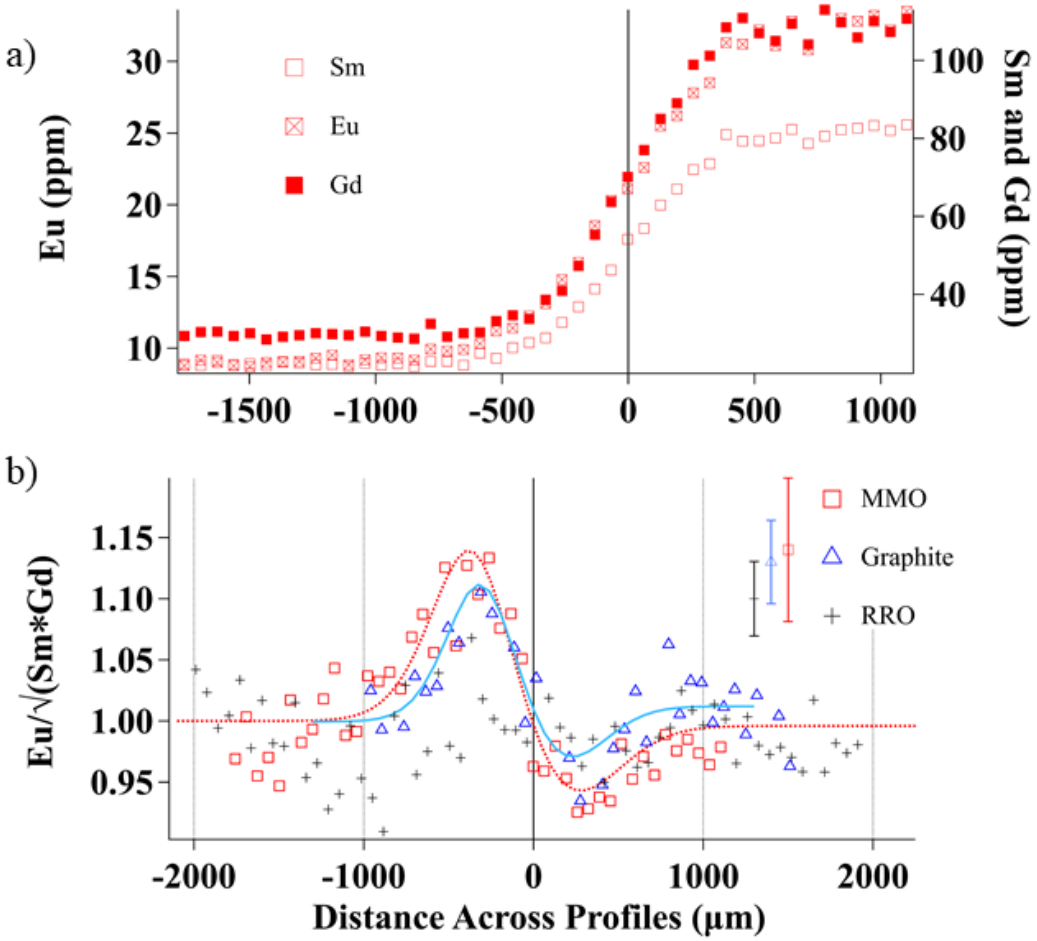

Fig. 6 (a, b): (a) Profiles of Sm, Eu and Gd for the 40 minute MMO buffered experiment. (b) A graph of the Eu Anomaly signal, $Eu/\sqrt{(Sm * Gd)}$ for the 40 minute experiments from each oxygen fugacity. The square (MMO) and triangle (graphite) markers are the experimental Eu anomaly signals. The dotted and solid lines are simulated ideal anomaly using the actual time and recovered experimental diffusivities as well $C_{-\infty}$, $C_{+\infty}$, from those experiments. The notched markers show the experimental data from the RRO experiment where no simulation is graphed as it does not have an identifiable Eu Anomaly. The average one S.E. on the experimental data points is shown in the right-hand corner. Both the simulation and experimental data have had their left-hand side normalized to one. For each dataset, the Eu/√(Sm*Gd)

value has been scaled by dividing by 0.356 which is an average of the first three datapoints on the left for each graph. This was done so that the signal can be graphed with Eu anomaly or Eu/√(Sm*Gd) relative to 1 on the y-axis.

Figure 7:

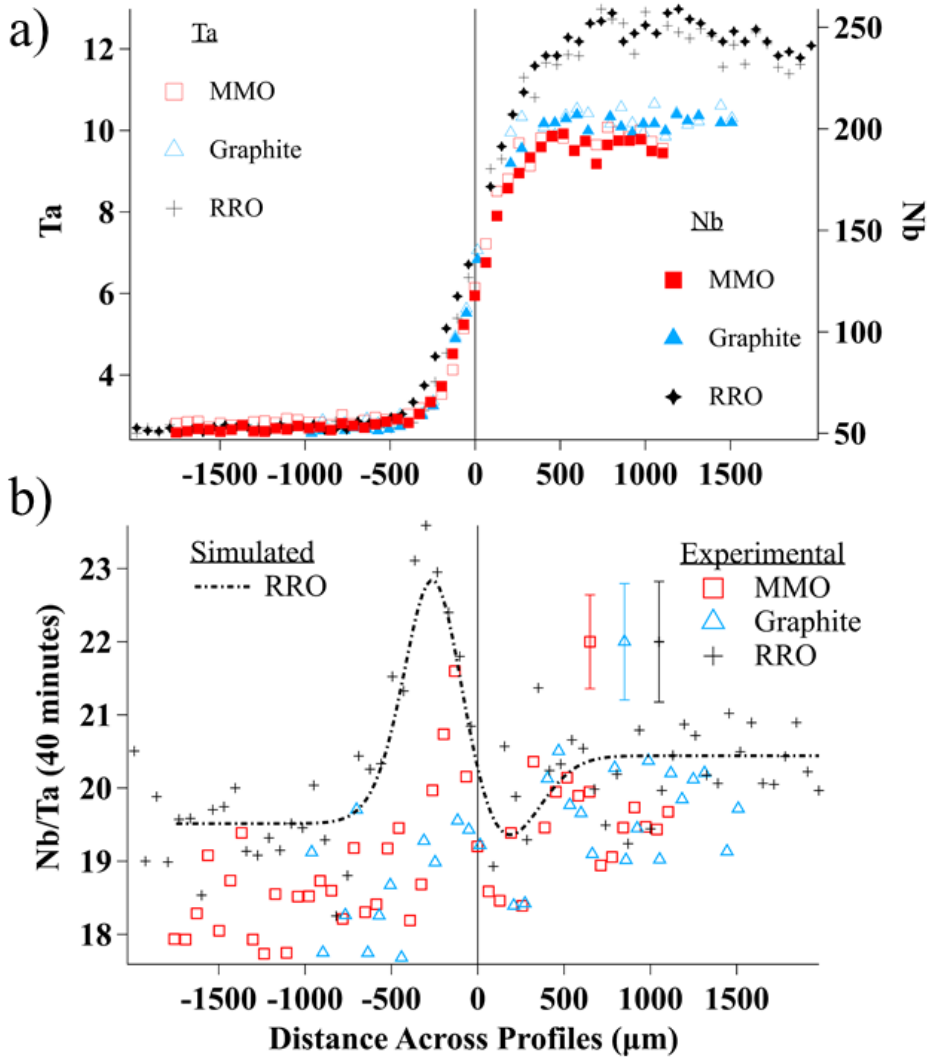

Fig. 7 (a, b): a) Profiles of Nb, Ta and b) the Nb/Ta ratio for the 40 minute experiments at RRO, MMO, and graphite. To aid in readability, error bars are presented as only an average of the 1 S.E. and are plotted on three fictitious points in the upper right corner of each plot. Similar to the "hill and trough" pattern in Eu/√(Sm*Gd), a subtle pattern of the same general shape can be seen in a graph of Nb/Ta. This pattern is observed in the 20 minute and 80 minute experiments as well so the 40 minute experiment is shown as representative. The simulation shown is based on the recovered diffusivities and concentrations of Nb and Ta in the 40 minute RRO experiment. There is also some starting fraction in Nb/Ta between

the different fO_2s in the low-trace element (left-hand) side that has some variation depending on fO_2. Examining the low-trace element side of b), this starting fraction is most noticeable when comparing the RRO Nb/Ta ratio to the MMO or graphite Nb/Ta ratio.

Figure 8:

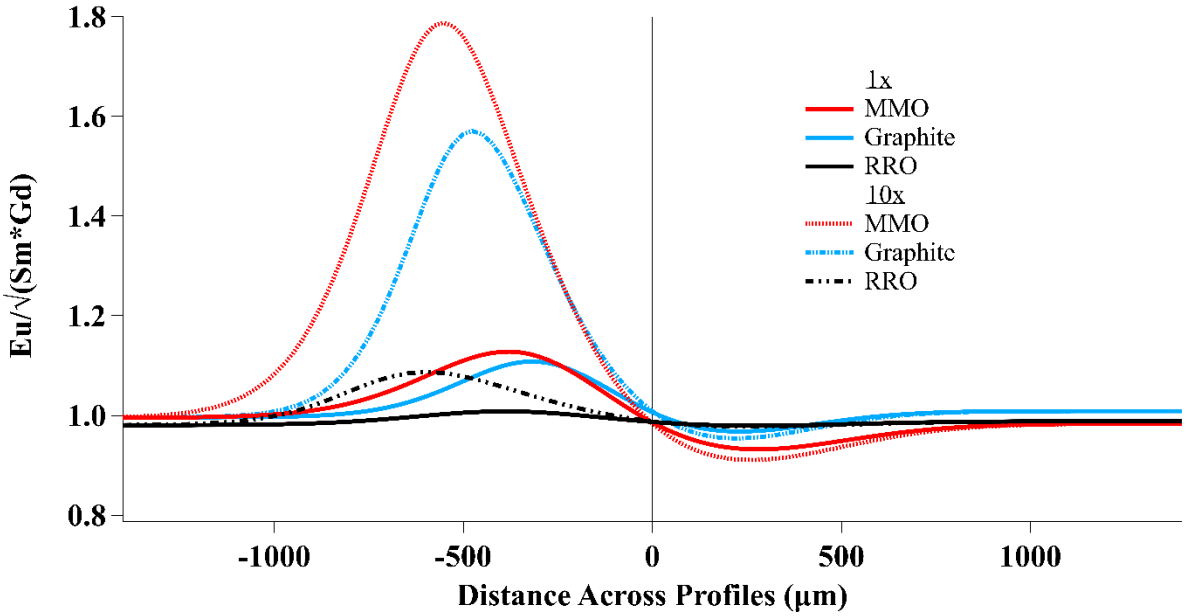

Fig. 8: Shows simulations of Eu fractionation when the concentration difference between the low-trace element and high-trace element is increased. Each profile is made with the diffusivities, $C_{-\infty}$ and $C_{+\infty}$ recovered from analysis of Sm, Eu, and Gd in the 40 minute experiments at each fO_2. The smallest curves represent no enrichment to $C_{+\infty}$ while the larger profiles represent a profile with 10*$C_{+\infty}$.

Figure 9:

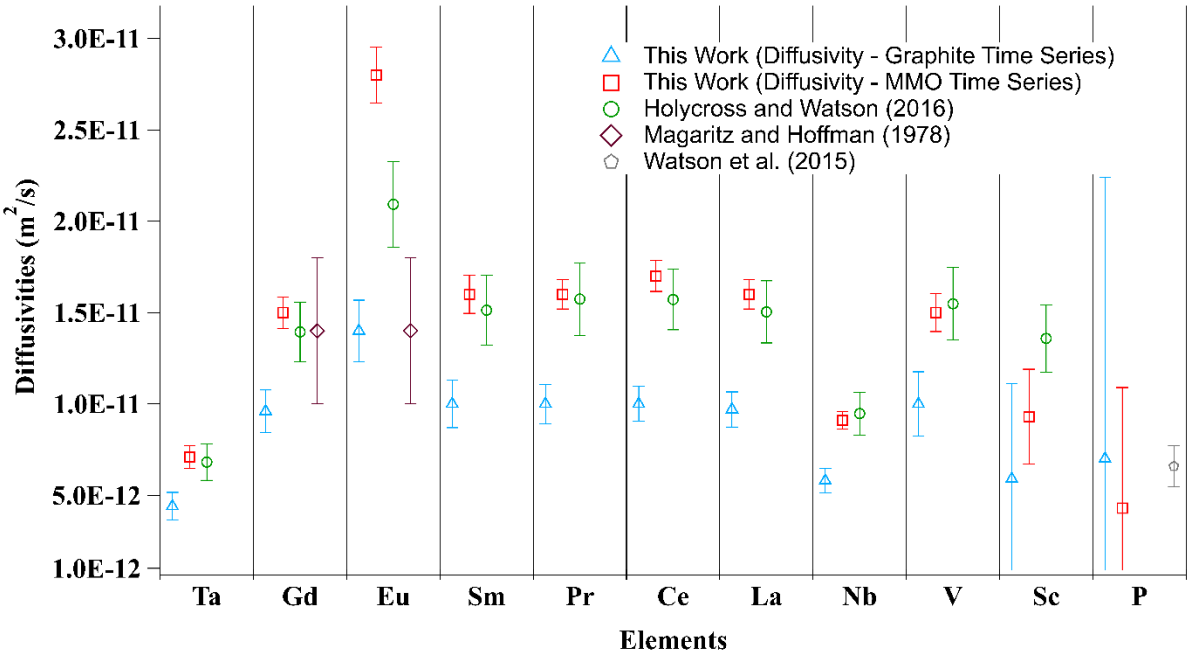

Fig. 9: Figure 8 is compares the preferred diffusivities in basalt from graphite capsule experiments and MMO-buffered experiments in this project with the diffusivities recovered by other workers. The preferred diffusivities from Table 4 are shown as well as their 2 times their standard errors. Holycross and Watson (2016) and Watson et al. (2015) present both the activation energy (E_a) and $\log D_0$ of trace elements in basalt and present 2σ standard errors on each of these values. Diffusivity for the elements from was calculated using the presented E_a and $\log D_0$ in the Arrhenius equation with 1300 C as the temperature.